Seismic structure of Cocos and Malpelo volcanic ridges and implications for hotspot-ridge interaction

V. Sallarès, P. Charvis, E. Flueh, J. Bialas

Seismic structure of Cocos and Malpelo Volcanic Ridges and implications for hot spot-ridge interaction

Valentí Sallarès and Philippe Charvis
Institut de Recherche pour le Développement, Géosciences Azur, Villefranche-sur-mer, France

Ernst R. Flueh and Joerg Bialas
Geomar, Research Center for Marine Geosciences, Kiel, Germany

Received 5 February 2003; revised 15 July 2003; accepted 10 September 2003; published 19 December 2003.

[1] The Cocos and Malpelo Volcanic Ridges are blocks of thickened oceanic crust thought to be the result of the interaction between the Galapagos hot spot and the Cocos-Nazca Spreading Center during the last 20 m.y. In this work we investigate the seismic structure of these two aseismic ridges along three wide-angle transects acquired during the Panama basin and Galapagos plume—New Investigations of Intraplate magmatism (PAGANINI)-1999 experiment. A two-dimensional velocity field with the Moho geometry is obtained using joint refraction/reflection travel time tomography, and the uncertainty and robustness of the results are estimated by performing a Monte Carlo-type analysis. Our results show that the maximum crustal thickness along these profiles ranges from ~16.5 km (southern Cocos) to ~19 km (northern Cocos and Malpelo). Oceanic layer 2 thickness is quite uniform regardless of total crustal thickness variations; crustal thickening is mainly accommodated by layer 3. These observations are shown to be consistent with gravity data. The variation of layer 3 velocities is similar along all profiles, being lower where crust is thicker. This leads to an overall anticorrelation between crustal thickness and bulk lower crustal velocity. Since this anticorrelation is contrary to crustal thickening resulting from passive upwelling of abnormally hot mantle, it is necessary to consider active upwelling components and/or some compositional heterogeneities in the mantle source. The NW limit of the Malpelo Ridge shows a dramatic crustal thinning and displays high lower crustal velocities and a poorly defined crust-mantle boundary, suggesting that differential motion along the Coiba transform fault probably separated Regina and Malpelo Ridges. *INDEX TERMS:* 3010 Marine Geology and Geophysics: Gravity; 3025 Marine Geology and Geophysics: Marine seismics (0935); 3035 Marine Geology and Geophysics: Midocean ridge processes; 7220 Seismology: Oceanic crust ; 8180 Tectonophysics: Tomography; *KEYWORDS:* seismic tomography, Galapagos hot spot, volcanic ridges

Citation: Sallarès, V., P. Charvis, E. R. Flueh, and J. Bialas, Seismic structure of Cocos and Malpelo Volcanic Ridges and implications for hot spot-ridge interaction, *J. Geophys. Res.*, *108*(B12), 2564, doi:10.1029/2003JB002431, 2003.

1. Introduction

[2] The presence of a hot spot near a spreading center enhances mantle melting along the ridge axis [*Morgan*, 1978]. The increased melt production results in thicker crust and shallower seafloor compared to normal spreading centers, as evidenced in the long-wavelength bathymetry and gravity anomalies extending hundreds of kilometers away from hot spots [*Schilling*, 1985; *Sleep*, 1990; *Ito and Lin*, 1995]. In addition, hot spot-related melting products generally exhibit distinct geochemical signature with respect to normal mid-oceanic ridge basalt (MORB) and are often referred to as ocean island basalt (OIB) [e.g., *Schilling et al.*, 1982; *Detrick et al.*, 2002].

0148-0227/03/2003JB002431$09.00

[3] A number of theoretical [*Ribe*, 1996; *Sleep*, 1990] and numerical [*Ito et al.*, 1996, 1999] studies have been conducted to investigate the dynamics of hot spot-ridge interaction. The amount of melting depends essentially on the volume flux of the plume, which is controlled both by (1) a passive (plate-driven) component, mainly a function of the mantle temperature and the spreading rate and (2) an active (plume-driven) component, which depends on the viscosity contrasts [e.g., *Ito et al.*, 1996]. Observational constraints on such complex dynamics, however, have been scarce so far.

[4] The Galapagos Volcanic Province (GVP) presents an excellent opportunity to investigate mantle melting processes associated with hot spot-ridge interaction. It is constituted by several blocks of thickened oceanic crust, which are believed to have been generated from the interaction between the Galapagos hot spot and the Cocos-Nazca Spreading Center (CNS) during the last 20 m.y. The most prominent

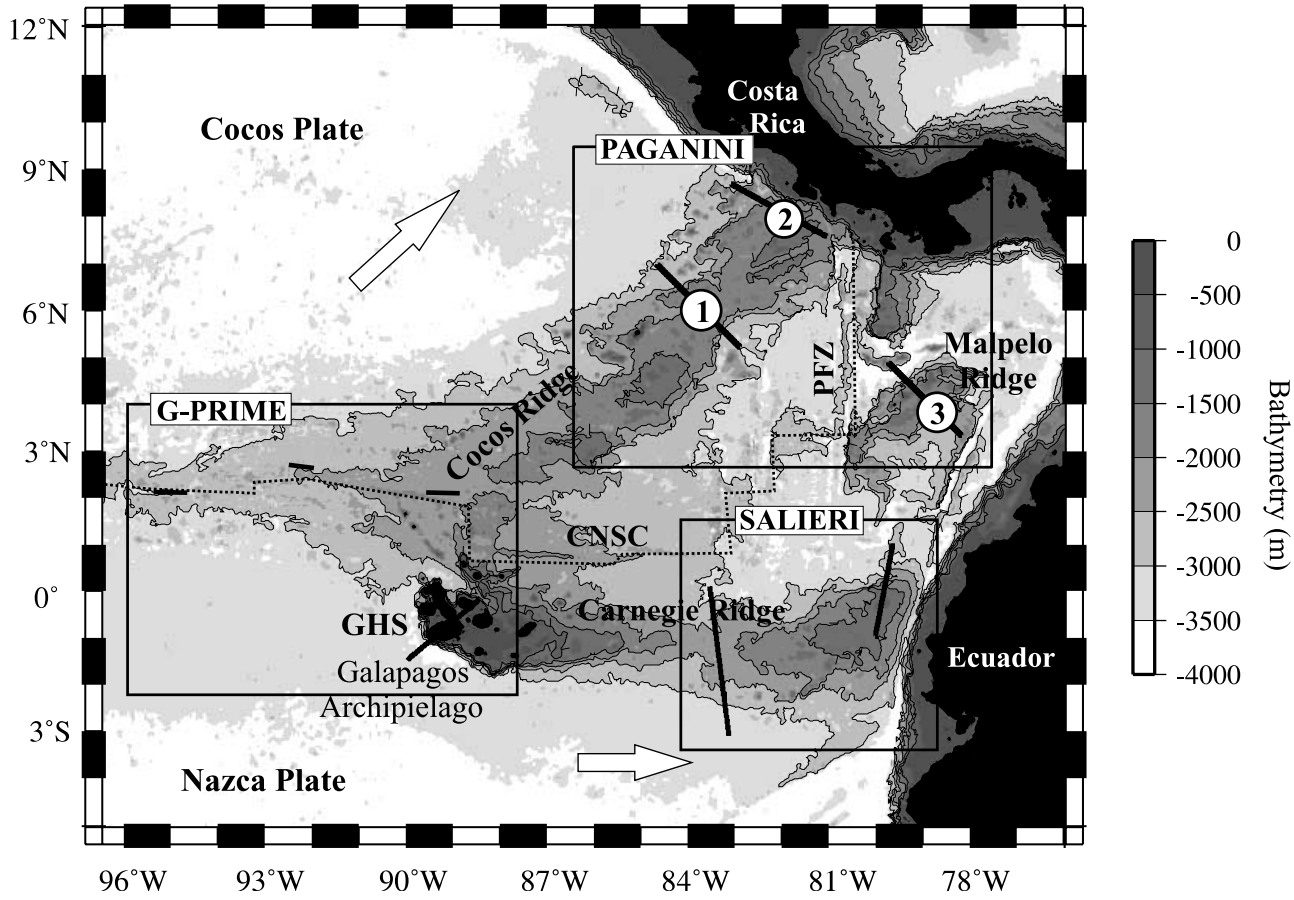

Figure 1. Bathymetric map of the Galapagos Volcanic Province (GVP) showing the main tectonic and geologic features of the area. Large arrows display plate motions relative to the stable South American craton [*DeMets et al.*, 1990]. Boxes outline the different seismic experiments recently performed in the area (PAGANINI-1999, G-PRIME-2000, SALIERI-2001), and black lines show location of all the wide-angle seismic profiles. Numbers indicate the seismic profiles used in this study. CNSC, Cocos-Nazca Spreading Center; GHS, Galapagos Hot spot; PFZ, Panama Fracture Zone.

are the Cocos, Malpelo, and Carnegie Ridges, which trace the path of the Galapagos hot spot over the Nazca and Cocos plates (Figure 1). The regional tectonic setting [*Hey*, 1977; *Lonsdale and Klitgord*, 1978; *Barckhausen et al.*, 2001], the plume-related mantle temperature anomalies [*Schilling*, 1991; *Ito and Lin*, 1995; *Canales et al.*, 2002], and the geochemical signatures of basalts along the CNS [*Schilling et al.*, 1982; *Detrick et al.*, 2002] and the volcanic ridges [*Harpp and White*, 2001] have been the object of numerous studies. Moreover, several seismic experiments have been conducted recently in this area, including the CNS [*Canales et al.*, 2002], the volcanic ridges [*Marcaillou et al.*, 2001; *Sallarès et al.*, 2002; *Trummer et al.*, 2002; *Walther*, 2002], and the Galapagos platform [*Toomey et al.*, 2001]. Proper interpretation of these seismic data will be essential to better understand the evolution of the hot spot-ridge interaction including the formation of the GVP.

[5] The main objective of this work is to obtain accurate 2-D velocity models along three wide-angle profiles acquired across the Cocos and Malpelo Ridges during the Panama basin and Galapagos plume—New Investigations of Intraplate magmatism (PAGANINI)-1999 seismic experiment. First, velocity models are determined using a joint refraction/reflection travel time inversion method [*Korenaga et al.*, 2000]. Second, the uncertainty and robustness of velocity models are estimated by performing a Monte Carlo-type analysis. The degree of velocity-depth ambiguities is checked by exploring the model space for different values of the depth kernel weighting parameter. Checkerboard tests are also conducted to estimate the resolving power of the data set. Third, the velocity models are converted to density models and compared with the free-air gravity data. Finally, the range of mantle melting parameters that can account for the estimated seismic structure is constrained on the basis of mantle melting models [*Korenaga et al.*, 2002], and their geodynamic implications are discussed.

2. Tectonic Setting

[6] The first consistent model of the GVP tectonic evolution was established by *Hey* [1977] and *Lonsdale and Klitgord* [1978] from reconstruction of magnetic anomalies and bathymetric data. This model suggests that major plate reorganization took place in the region around 25 Ma, breaking the ancient Farallon plate into the Cocos-Nazca

plate (south) and the Juan de Fuca plate (north) [*Hey*, 1977]. Because of differential stresses between the northeastward subducting Cocos segment and the eastward subducting Nazca segment, rifting was initiated at about 23 Ma between both segments near the Galapagos hot spot, evolving later into N-S seafloor spreading along the CNS and originating both Nazca and Cocos plates [*Hey*, 1977; *Lonsdale and Klitgord*, 1978]. The Grijalva Scarp, an old N60°E fracture zone, is thought to represent the southern half of the scar where the Farallon plate was cut off. The V-shaped Carnegie and Cocos Ridges outline the motion of the Galapagos hot spot over the east trending Nazca plate and the northeast trending Cocos plate, respectively [*Pennington*, 1981; *Kolarsky et al.*, 1995]. Carnegie and Cocos Ridges separated from one another during a continuous period of rifting and seafloor spreading between ~23 and 9 Ma [*Hey*, 1977; *Lonsdale and Klitgord*, 1978]. Kinematic reconstructions suggest that the Malpelo Ridge is a former continuation of the Cocos Ridge, which was split by dextral motion along the N-S trending Panama Fracture Zone (PFZ). This fracture zone initiated at about 9 Ma, as a consequence of the blocking of the Cocos plate subduction beneath Middle America [*Sallarès and Charvis*, 2003]. Hence, from 9 Ma to the present, N-S seafloor spreading has continued between the Cocos and Carnegie Ridges west of the PFZ, but not along the eastern segment [*Hey*, 1977; *Pennington*, 1981]. Motion along the PFZ is also suggested to have induced N-S extensional stresses in the northeastern part of the Nazca plate, resulting in the separation of the original Malpelo Ridge into several smaller ridges (current Malpelo, Regina, and Coiba). The initial rift would have evolved later into the currently E-W trending Coiba transform fault [*Lonsdale and Klitgord*, 1978], so the small block located between Coiba transform fault to the south, Panama to the north, Colombian trench to the east, and PFZ to the west may be interpreted at present as an independent microplate (Figure 2). Both active and extinct rifts of the CNS as well as fracture zones and transform faults are expressed in the bathymetry (Figure 1). The age of the Cocos Ridge subducting at the trench is 14–15 Ma based on radiometric data [*Hoernle et al.*, 2000], and the ages of Carnegie Ridge at the trench and the conjugate Malpelo Ridge are estimated to be ~20 Ma from magnetic anomalies reconstruction [e.g., *Lonsdale and Klitgord*, 1978].

[7] At present-day, the CNS lies about 190 km north of the Galapagos hot spot, and its full spreading rate varies from 45 to 68 km/m.y. between 85°W and 96°W on the basis of global plate motion model NUVEL-1[*DeMets et al.*, 1990]. Seafloor spreading along the CNS is thought to have been roughly symmetric during the last 20 m.y., as confirmed by *Wilson and Hey* [1995] and *Barckhausen et al.* [2001]. The hot spot began accreting the Cocos and Carnegie Ridges at ~23 Ma, not far from the CNS [*Hey*, 1977; *Barckhausen et al.*, 2001]. Since then, the CNS is thought to have moved toward the north at ~26 km/m.y. with respect to the hot spot, thus a similar velocity to the half spreading rate [*Sallarès and Charvis*, 2003]. The CNS migration, combined with ridge jumps and variations in the full spreading rate, have resulted in temporal variations on the relative location of the hot spot with respect to the spreading center. Different geophysical data indicate that at ~20 Ma the hot spot was approximately ridge centered and at ~15 Ma a southward ridge jump placed the hot spot beneath the Cocos plate [*Barckhausen et al.*, 2001; *Sallarès and Charvis*, 2003]. Eventually, at ~7.5 Ma, the hot spot crossed the CNS toward its present location beneath the Nazca plate [*Wilson and Hey*, 1995; *Sallarès and Charvis*, 2003].

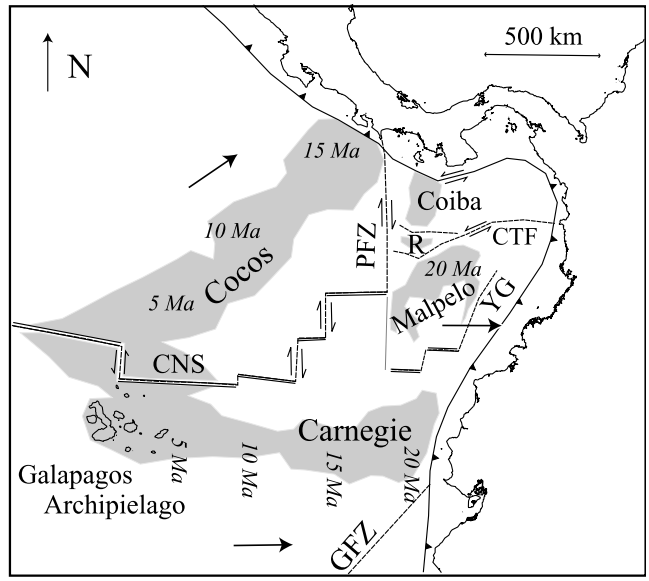

Figure 2. Schematic tectonic map of the study area, showing the most prominent geological and tectonic features, and the estimates of lithospheric age based on absolute plate motions. Arrows indicate the relative plate motions [*DeMets et al.*, 1990]. CTF, Coiba Transform Fault; CNS,: Cocos-Nazca Spreading Center; GFZ, Grijalva Fracture Zone; PFZ, Panama Fracture Zone; R, Regina Ridge; YG, Yaquina Graben. Seafloor ages are based on reconstruction of magnetic anomalies [*Lonsdale and Klitgord*, 1978].

3. Wide-Angle Seismic Data

[8] The data set used in this study is composed of ocean bottom data from three wide-angle seismic profiles acquired in summer 1999 during the PAGANINI cruise aboard the R/V *Sonne* (Figure 1). Shooting along these profiles was conducted using up to three 2000 cubic inch air guns, although due to technical problems only two air guns were used most of the time. The firing interval was set at 60 s, which at 4.5 knots means a shot spacing of ~140 m. The set of receivers was composed of 21 Geomar ocean bottom hydrophones (OBH) and ocean bottom seismometers (OBS), 13 IRD OBS, and 1 Ifremer OBH. The OBS and OBH were deployed along one line of 245 km (profile 3, Malpelo, 27 instruments), another one of 260 km (profile 2, northern Cocos, 27 instruments), and a third one of 275 km (profile 1, southern Cocos, 21 instruments), with a receiver spacing ranging from 5 to 12 km. The location of the seismic lines is shown in Figure 1.

[9] Most of the data along the three profiles are of high quality, showing clear intracrustal refractions (*Pg* phases) and crust-mantle boundary reflections (*PmP*) up to offsets of ~150 km from the sources (Figure 3). In the northernmost instruments of profile 3 (0–50 km along profile), we

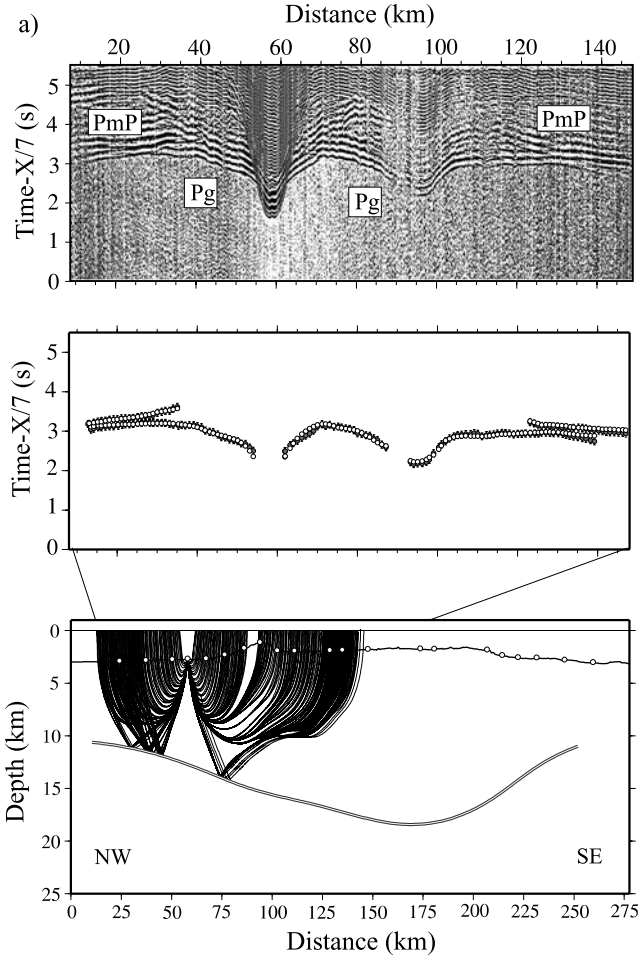

Figure 3a. OBS 4, profile 1. (top) Several examples of wide-angle seismic data along the three transects, plotted after automatic gain correction, 5–15 Hz Butterworth filtering, deconvolution, and equalization. (middle) Picked travel times (solid circles with error bars) and predicted travel times (open circles) for *Pg* and *PmP* phases. (bottom) Ray tracing for all identified seismic phases. Ray paths and synthetic travel times are calculated using the velocity models displayed in Figure 5.

also identified and used the upper mantle refraction (*Pn*) (Figure 3g), but not in profiles 1 and 2. The basic data processing consisted of a 5–15 Hz Butterworth filtering and automatic gain control. Equalization and predictive deconvolution were also applied to the record sections in order to improve the signal-to-noise ratio.

[10] The *Pg* phase is clearly observed in all the record sections. The pattern of this phase is similar in most of the instruments from the three lines, though some strong lateral variations related with prominent bathymetric features are also observed. At near offsets, it shows low apparent velocities (4–6 km/s), which increase strongly with distance to reach velocities of around 7.0 km/s at ~20 km from the source (Figure 3). This is consistent with a refraction within the upper igneous crust (oceanic layer 2), where the vertical velocity gradient is high due to porosity reduction as well as more subdued hydrothermal alteration with depth [e.g., *Detrick et al.*, 1994]. At farther offsets (typically >20 km), the apparent velocity of *Pg* phases looks almost uniform, and rarely exceeds 7.0 km/s. The long (more than 100 km) and flat tail of this phase is interpreted to be a refraction within the upper part of the lower crust (oceanic layer 3). The small velocity gradient within layer 3 prevents seismic rays to turn deep inside this layer.

[11] The reflection phase from the crust-mantle boundary (*PmP*) is also observed in most of the record sections from all three lines with variable quality. In the deep ocean basins (e.g., at both edges of profile 3), *PmP* is observed at near offsets (~20 km), and *PmP* and *Pg* become indistinguishable at about 40 km from the source (Figure 3a). This is consistent with a reflection from the Moho of an oceanic crust with normal crustal thickness (7–8 km). In contrast, in the receivers located at the crest of the ridge, *PmP* phases are much more energetic and easier to identify than in the flanks, indicating the presence of a better developed crust-mantle boundary (Figure 3c).

[12] In order to identify the seismic phases consistently in all record sections, we checked the reciprocity of travel times for a number of source-receiver pairs. Picking of *Pg* and *PmP* phases was done manually, and picking errors were assigned on the basis of the dominant period and the quality of the phase. Typically, errors were assumed to be half a period of one arrival, to account for a possible

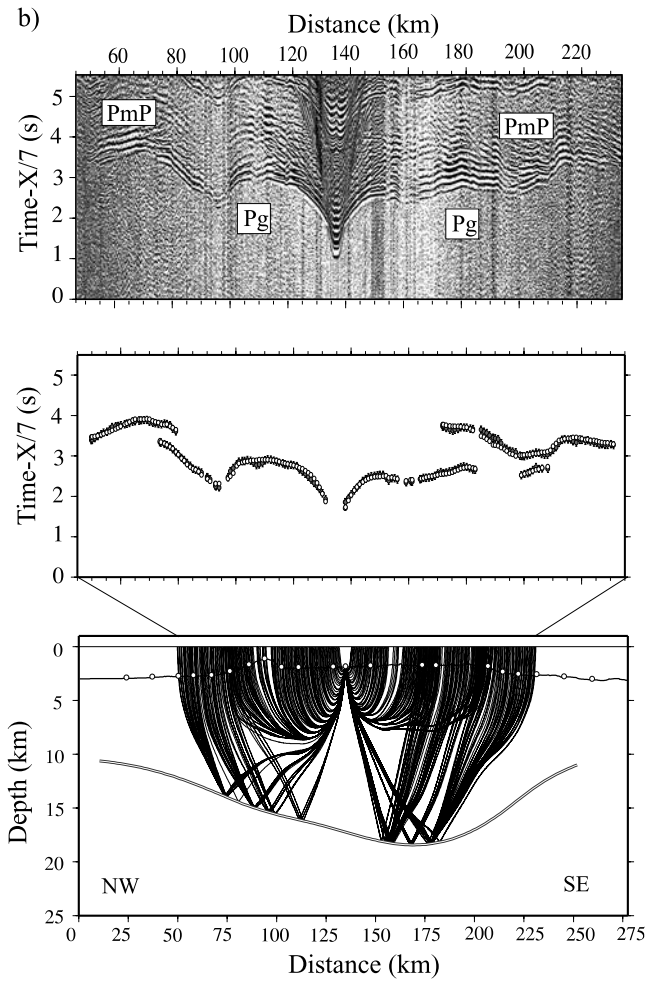

Figure 3b. Same as Figure 3a for OBS 12, profile 1.

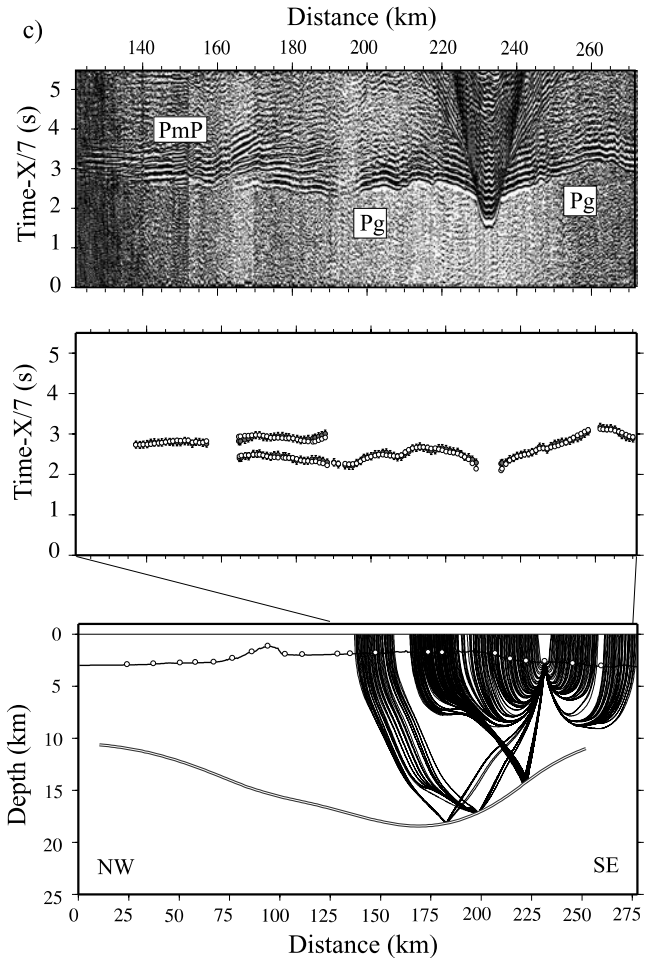

Figure 3c. Same as Figure 3a for OBS 19, profile 1.

systematic shift in the arrival identification, and these errors were overweighted or downweighted depending on the phase quality. Errors are about 40–50 ms at near offsets and 60–70 ms at far offsets for *Pg* and *Pn* phases, while for *PmP* phases an average error of 70–90 ms was assigned.

4. Travel Time Tomography

4.1. Method

[13] Two-dimensional velocity models along the three profiles were calculated using the joint refraction and reflection travel time inversion method of *Korenaga et al.* [2000]. This method allows determining a 2-D velocity field and the geometry of a floating reflector from the simultaneous inversion of first arrival and reflection travel times. The 2-D velocity field is parameterized as a mesh of nodes hanging from the seafloor, and the node spacing can vary laterally and vertically. The floating reflector is represented as an independent array of linear segments with only one degree of freedom (vertical) for each reflector node. In this study the floating reflector is used to model the crust-mantle boundary. The forward problem for both refracted and reflected phases is solved using a hybrid ray-tracing scheme based on the graph method [*Moser*, 1991] with a local ray-bending refinement [*Moser et al.*, 1992]. Smoothing constraints using predefined correlation lengths and optional damping constraints for the model parameters are employed to regularize an iterative linearized inversion. For further details of this method, see *Korenaga et al.* [2000].

[14] Owing to the nature of the joint refraction/reflection inverse problem, there are three issues that have to be addressed before any interpretation of the results. The first issue is related to the nonuniqueness of the inversion solution, which makes that the final solution depends on the starting velocity model. The degree of dependence depends on the method of linearization and the geometry of the experiment, and must be assessed by conducting a number of inversions with a variety of initial models. The second issue concerns the trade-off between depth and velocity parameters in reflection tomography [e.g., *Bickel*, 1990], which depends on the source-receiver geometry. A conventional procedure to estimate the degree of velocity-depth ambiguities is to perform sensitivity tests using synthetic data for a given source-receiver geometry (i.e., checkerboard tests). However, checkerboard tests are known to be only a limited demonstration of velocity-depth ambiguities, since they just show the sensitivity of the method and the data set to very specific velocity models with particular anomalies located at determined places. Instead, *Korenaga et al.* [2000] proposed to explore the solution space systematically by changing the value of the

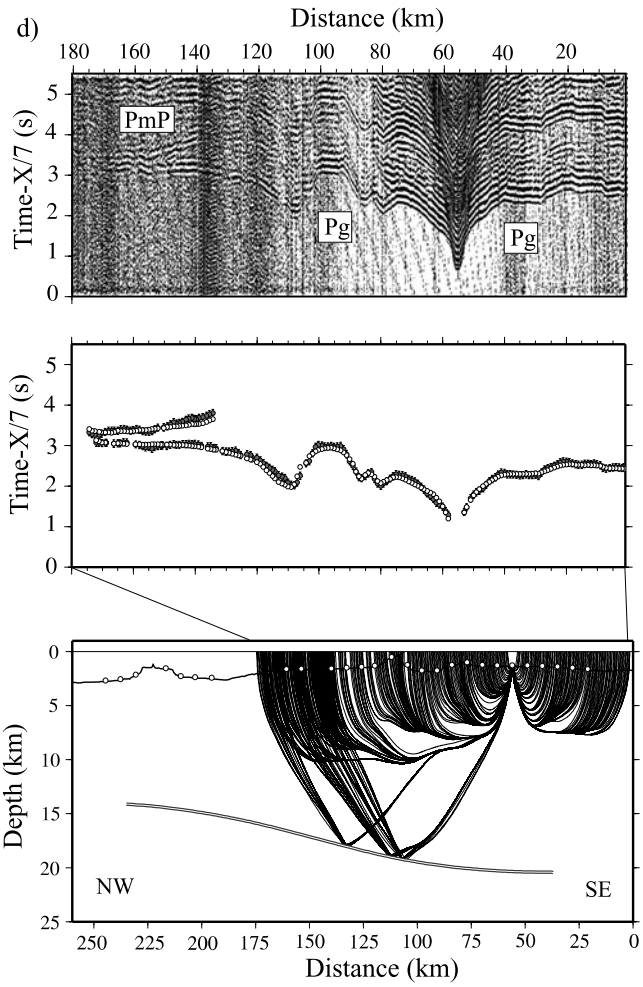

Figure 3d. Same as Figure 3a for OBS 6, profile 2.

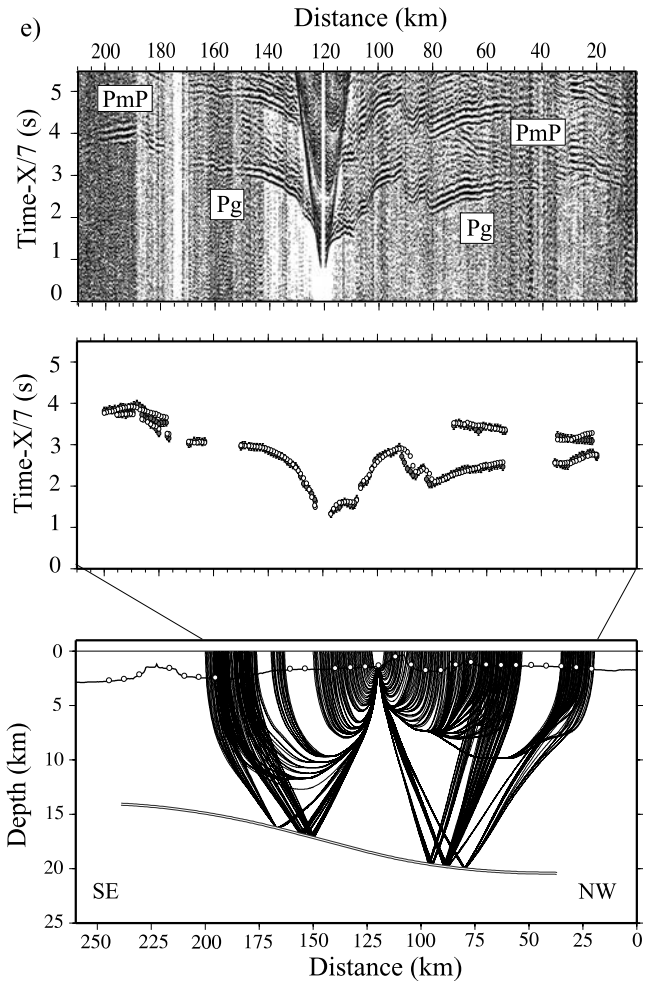

Figure 3e. Same as Figure 3a for OBS 15, profile 2.

depth kernel weighting parameter (w), which controls the relative weighting of velocity and depth parameters in the reflection travel time inversion. If trade-off is not significant, different values of w should lead to similar solutions. On the contrary, if the system is singular, increasing the weighting parameter should lead to larger depth perturbations with smaller velocity perturbations (and vice versa). The velocity-depth ambiguity can thus be tested by systematically exploring the solution space with this single control parameter, as indicated by *Korenaga et al.* [2000].The third issue concerns the estimate of the model uncertainties, which is essential to relate confidently seismic velocities with rock composition. A practical way to estimate uncertainties for a nonlinear inversion is to perform a Monte Carlo analysis [e.g., *Tarantola and Valette*, 1982; *Tarantola*, 1987]. If we invert data with random errors for N random initial models, assuming that all N realizations have the same probability ($1/N$), the a posteriori covariance matrix of the set of Monte Carlo realizations can be expressed as follows [*Matarese*, 1993],

$$C \approx \frac{1}{N} \sum [p_i - E(p)][p_i - E(p)]^T,$$

where p_i is the solution of the ith realization and $E(p)$ denotes the a posteriori expectation of model parameters.

[15] In order to resolve these issues of the inverse problem, we conducted an inversion procedure composed of the following steps: (1) the estimation of a 1-D average model, (2) the generation of a set of 1-D initial Monte Carlo ensembles, and (3) the iterative inversion for all the ensembles.

[16] To derive the 1-D average model, bathymetry-corrected travel times from all record sections along a given profile are mapped into a single travel time/offset diagram, and a third order polynomial regression is performed for first arrivals and *PmP* travel times (Figure 4a). The bathymetric correction consists in subtracting the travel time spent by a seismic ray from the seismic source to the sea bottom from the total travel time. The remaining travel time is that spent by the ray within the earth's interior. The 1-D average model is defined here to be the one that gives the best fit of the polynomial model (the lowest root-mean-square, RMS) (Figures 4b and 4c). The velocity beneath the Moho is fixed after each iteration and corresponds to that of the node located immediately above the Moho. In order to perform the Monte Carlo analysis, a set of 100 1-D initial models is constructed by randomly varying the Moho depth (σ_d = 3 km) and the velocity (σ_v = 0.3 km/s) into several nodes at representative depths of the 1-D average model (Figure 4c). In addition, 100 different data sets are built by

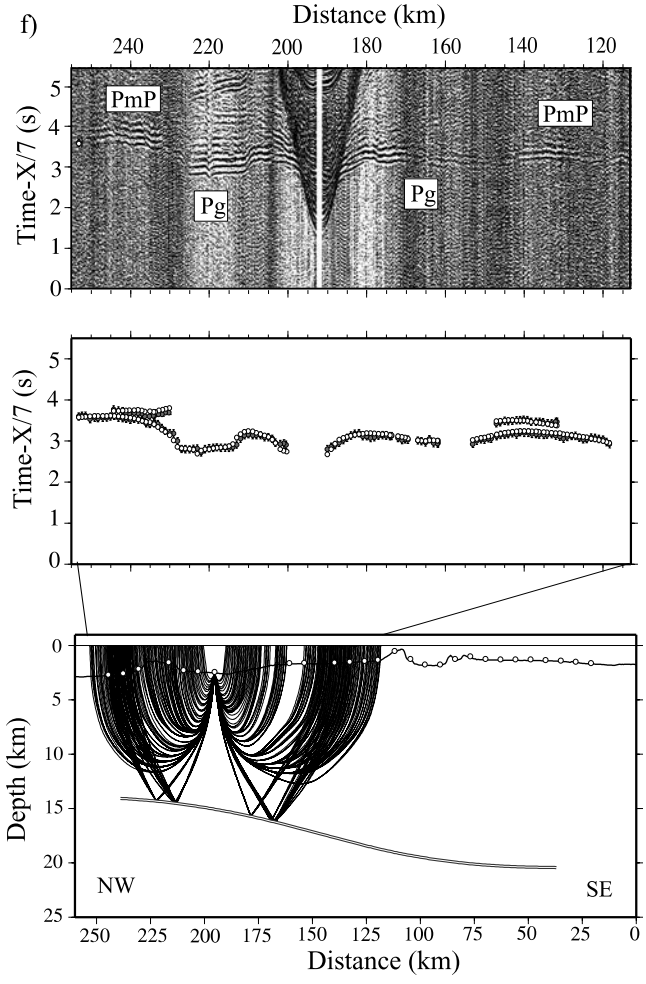

Figure 3f. Same as Figure 3a for OBS 21, profile 2.

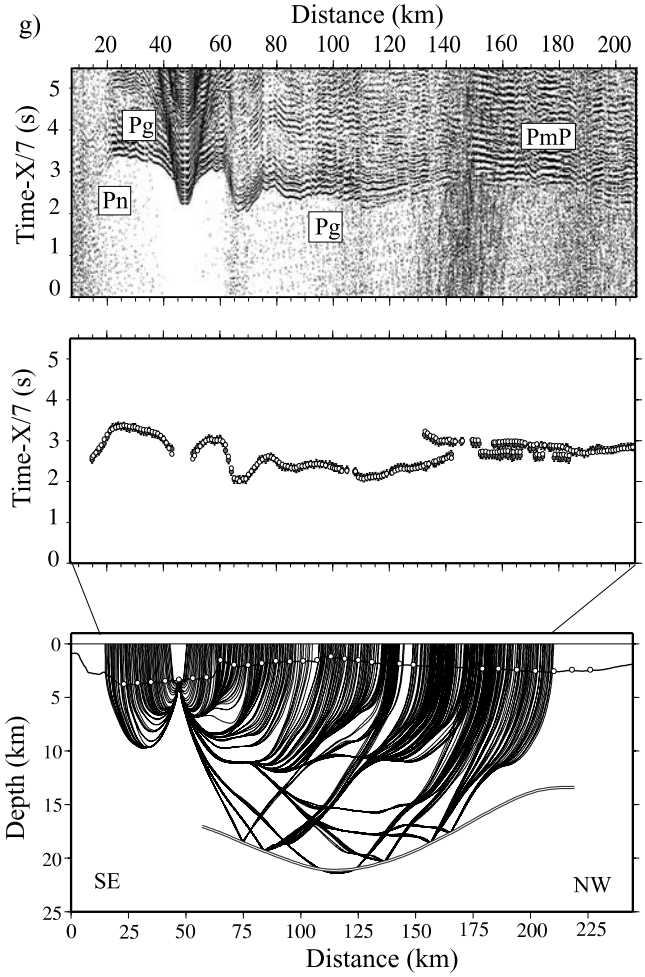

Figure 3g. Same as Figure 3a for OBS, profile 3.

adding random phase gradient errors (±50 ms) and common receiver errors (±30 ms) to the initial data set [*Zhang and Toksöz*, 1998]. Finally, a 2-D inversion is performed for each random initial model with a random data set. We adopt the average of all the Monte Carlo realizations (i.e., the a posteriori expectation) as final solution. Mean deviations of velocity and depth parameters from such an ensemble average can be interpreted as a measure of model uncertainties (the a posteriori variance). In order to estimate the robustness of the obtained solution at the different depth levels, we have compared the horizontally averaged uncertainty of the velocity models before and after the inversion.

4.2. Results

4.2.1. Inversion Parameters

[17] On profile 1 (Figure 1), a total of 3830 *Pg* and 1898 *PmP* travel times from 21 record sections were picked. The model is 275 km wide and 30 km deep. Horizontal grid spacing is 0.5 km, whereas vertical grid spacing is varied from 0.2 km at the top of the model to 1.5 km at the bottom. Depth nodes are 1 km spaced. We used horizontal correlation lengths ranging from 4 km at the top to 10 km at the bottom and vertical correlation lengths varying from 0.4 km at the top to 2.5 km at the bottom. This is the minimum size of anomalies which may be resolvable with the data set at the different depths on the basis of a number of previous tests. We have also tested other values for the correlation lengths, but we found that varying this value by 50% does not affect significantly to the obtained model. As indicated by *Korenaga et al.* [2000], there is a trade-off between correlation lengths and smoothing weights, and we tried to use shorter correlation lengths with larger smoothing weights in order to reduce memory requirements. The depth kernel weighting parameter is $w = 1$, which means that depth and velocity nodes are equally weighted for the *PmP* travel time inversion. The 1-D average model and the 100 random initial models obtained in this profile are shown in Figures 4b and 4c. The RMS travel time misfit using the 1-D average model is 397 ms ($\chi^2 \sim 36$), and for the final model (after eight iterations) it is 65 ms ($\chi^2 \sim 1.1$). On profiles 2 and 3 (Figure 1), 5709 *Pg* and 1649 *PmP* and 7711 *Pg* and 2495 *PmP*, respectively, from 27 record sections were picked. The models for profiles 2 and 3 are both 30 km deep and are 260 km wide and 245 km wide, respectively. Since the dimensions of these two models are comparable to those of profile 1, they have been parameterized using the same vertical and horizontal node spacing and the same correlation lengths as in profile 1. The RMS misfit using the 1-D average model is 466 ms ($\chi^2 \sim 49$) for profile 2 and 439 ms ($\chi^2 \sim 74$) for profile 3, and for the final

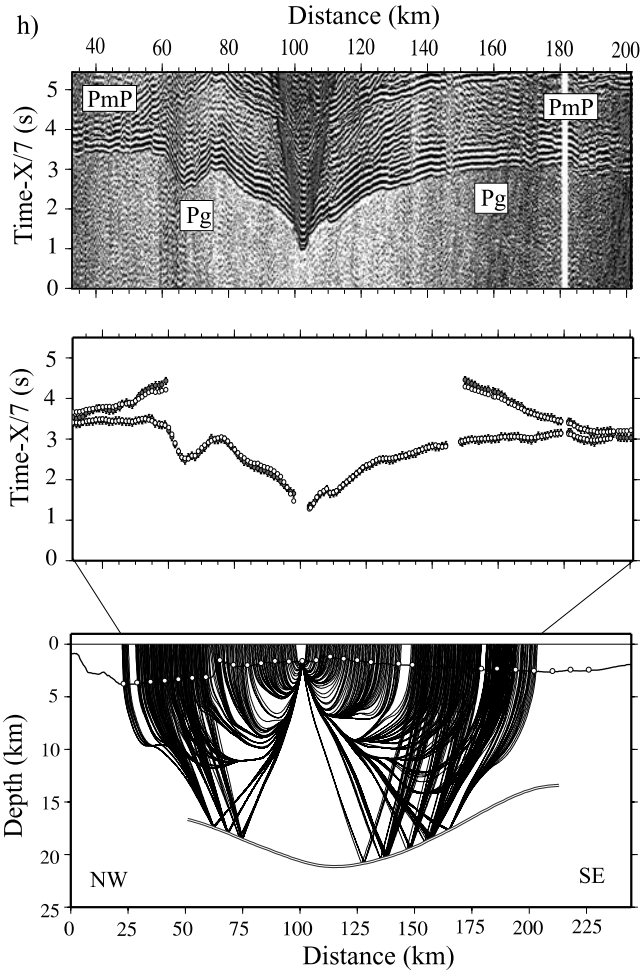

Figure 3h. Same as Figure 3a for OBS 14, profile 3.

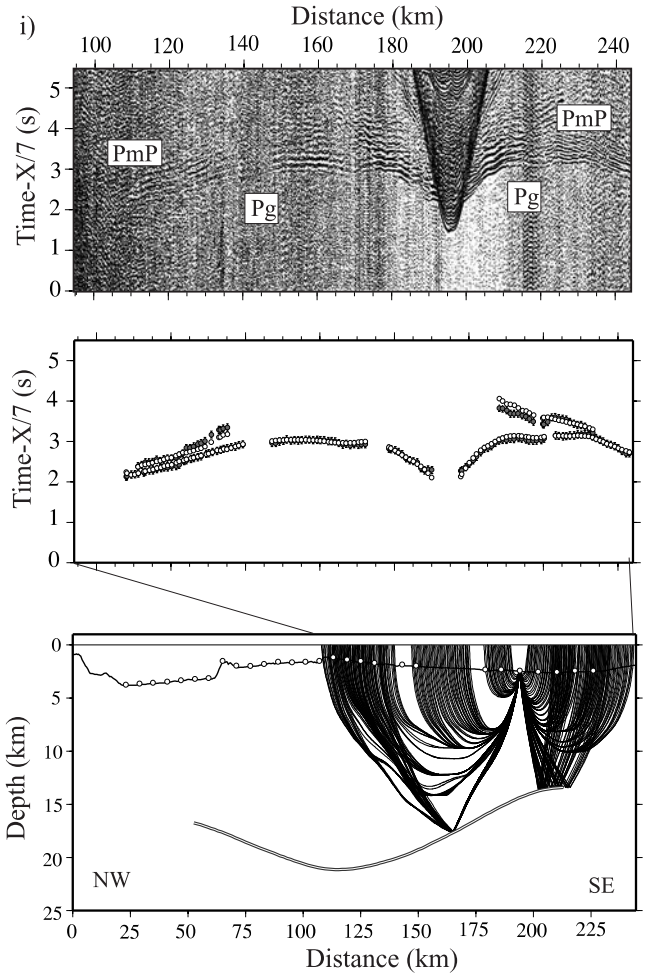

Figure 3i. Same as Figure 3a for OBS 24, profile 3.

model they are 71 ms (χ^2 ~1.3) and 67 ms (χ^2 ~1.1), respectively.

[18] The fit between inverted and observed travel times in several instruments along these lines is shown in Figure 3, together with corresponding ray tracing of *Pg* and *PmP* phases. The final (average) models of all the Monte Carlo realizations are shown in Figure 5. The derivative weight sum (DWS) corresponding to these models is shown in Figure 6. This parameter is the column sum vector of the velocity kernel [*Toomey and Foulger*, 1989], which provides crude information on the linear sensitivity of the inversion.

4.2.2. Seismic Structure

[19] The crustal structure obtained along the three profiles is quite similar (Figure 5). In terms of seismic velocities, it is constituted of two different layers. The upper layer is characterized by large vertical velocity gradients, with velocities typically ranging from 3.0–3.5 km/s at the top of the layer to ~6.5 km/s at the bottom. We have identified this layer to be the oceanic layer 2. In the long-wavelength structure, the thickness of the layer (3.5 ± 0.5 km) is quite uniform regardless of total crustal thickness. The bottom of layer 2 is defined here to be the point of maximum velocity gradient variation. In order to avoid short-wavelength local variations, this interface has been calculated for a long-wavelength, laterally averaged model (i.e., with a 25 km wide moving window). It is shown as a dashed line for the three profiles in Figure 5. The layer lying below this boundary up to the Moho interface is considered to be the oceanic layer 3. Unlike layer 2, the thickness of this layer is highly variable, ranging from ~4 km in the oceanic basins to ~15 km in the thickest crustal segments. Therefore layer 3 mostly accommodates the crustal overthicknening. It is characterized by a nearly uniform velocity, with velocities rarely exceeding 7.2–7.3 km/s. An interesting feature, which is systematically observed along the three profiles, is that average layer 3 velocities tend to be lower where the crust is thicker.

[20] Major differences among the three profiles are the geometry of the crust-mantle boundary and its transition toward the adjacent oceanic basins. In profile 1, the maximum crustal thickness of ~16.5 km is obtained beneath the crest of the ridge (Figure 5a). In contrast, the crustal thickness at the adjacent oceanic basins (i.e., at both ends of the profile) is 7–8 km, similar to that of a normal oceanic crust. The Moho geometry is asymmetric, showing a relatively sharp transition from thickened to normal crust in the SE limit of the profile and a smoother transition in the NW limit. In profile 2, the maximum crustal thickness (~18.5 km) is obtained at the NE limit of the transect (Figure 5b). As opposed to profile 1, this line does not reach a normal oceanic basin, as evidenced by the numerous seamounts observed in the southwestern flank of the ridge. The thinnest crust (~11 km) here is notably thicker than normal oceanic crust. In profile 3, the maximum crustal thickness of ~19 km is found beneath the crest of the ridge (Figure 5c). The geometry of the crust-mantle boundary is highly asymmetric. Toward the SE part of the profile, a smooth transition to a thinner crust of ~11 km is observed. The NW part, in contrast, shows a much sharper transition. The lack of *PmP* reflections makes it difficult to locate precisely the crust-mantle boundary from 0 to 75 km along profile (Figure 3g), but a shallow mantle-like velocity body (V_p ~7.9–8.0 km/s) located in this flank of the ridge as constrained by *Pn* travel times in this particular section of the profile, indicates that crustal thickness here (~6 km) is almost normal. Layer 2 thickness is very similar to that of the other two profiles along most of the profile, but not in the NW flank, where layer 2 is significantly thinner than in the rest of the profile (~2.0 km). Toward the SE the velocity increase for layer 3 is comparable to that observed in the flanks of the other two profiles, but toward the NW this variation is much faster coinciding with the sharp crustal thinning and with a pronounced bathymetric scarp (Figure 5c).

4.3. Model Uncertainties and Sensitivity Tests

[21] The uncertainties of the model parameters based on the Monte Carlo ensembles are shown in Figure 6. Results are quite similar in all transects, showing velocity uncertainties smaller than 0.05 km/s within most parts of the models. Interestingly, velocity uncertainties are generally larger above 5–6 km depth (0.05–0.10 km/s) than beneath this level. This is in agreement with the high velocity gradients of oceanic layer 2, which make that small changes in the travel time picking (even within the limits of the travel time uncertainties) can lead to notable variations in the absolute seismic velocities. In the lower part of the crust,

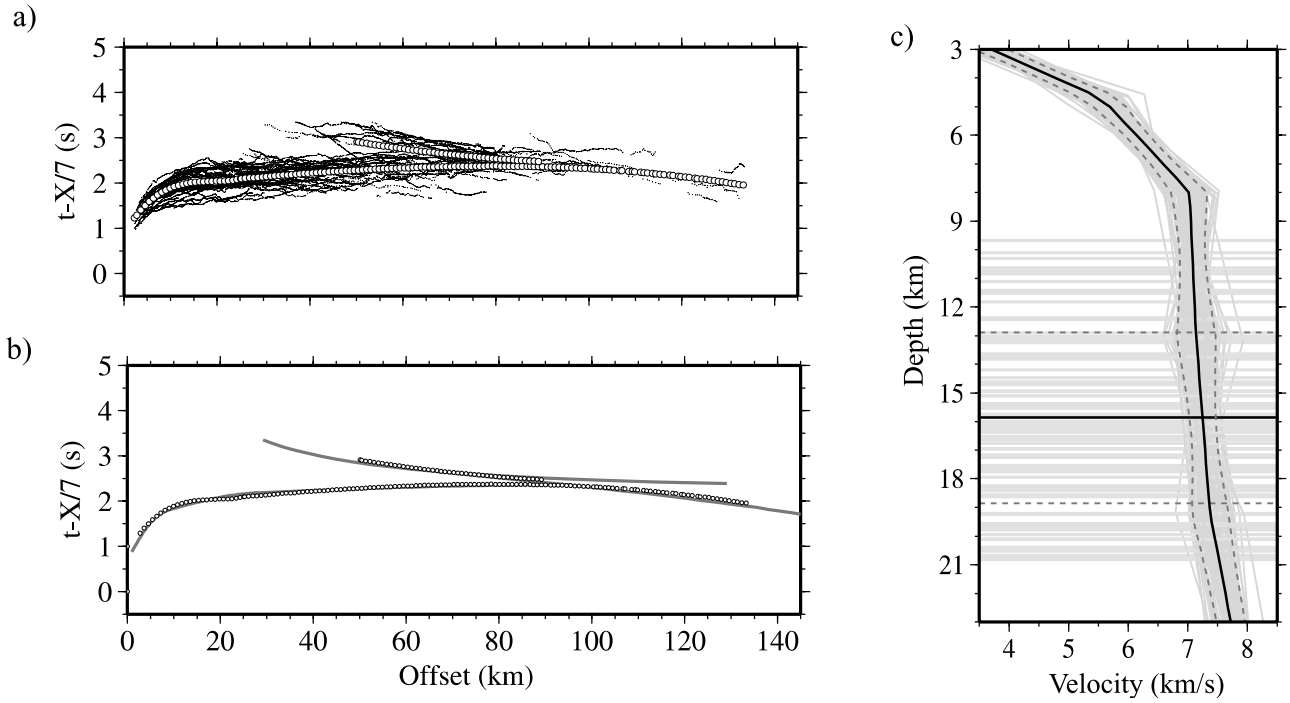

Figure 4. (a) Bathymetry-corrected travel time picks from all instruments along profile 1, southern Cocos plotted versus offset (solid circles) and results of cubic regression (open circles). (b) Results of cubic regression (open circles) and predicted travel times from the 1-D average model (grey lines). (c) The 1-D average model and corresponding Moho depth (solid black lines). Solid grey lines show all 100 random initial velocity and Moho depth models used for the Monte Carlo analysis. Dashed lines show the mean deviation for model parameters.

which is basically imaged by *PmP* phases, uncertainties are slightly larger than in the upper crust (around 0.1–0.15 km/s), although they are smaller than 0.2 km/s. For depth parameters, uncertainties are lower than 0.5 km along most parts of the models. Typically, the largest velocity uncertainties within the lower crust are consistently correlated with the largest depth uncertainties for the Moho reflector. This is evident in the thickest part of profiles 1 and 2 (Figures 6a and 6c), where velocity uncertainties over 0.15 km/s and depth uncertainties of 0.5–0.6 km/s are found. In the NW limit of profile 3, this correlation is even stronger, showing velocity uncertainties of 0.15–0.2 km/s and depth uncertainties higher than 1.5 km (Figure 6e). Consistently, in this part, *PmP* reflections are lacking or hard to identify (e.g., Figure 3g).

[22] In order to check the degree of velocity-depth ambiguities, we repeated the inversion for the three profiles using the average 1-D model as initial model but with different values for the depth kernel weighting parameter. The results obtained for profile 3 using $w = 0.1$ (which allows more velocity perturbations than depth perturbations), $w = 1$ (same weight to depth and velocity perturbations), and $w = 10$ (more depth perturbations than velocity perturbations) are shown in Figure 7. The obtained models and travel time misfits are very similar, and the velocity and Moho depth differences are lower than the model uncertainties shown in Figure 6. Results along the other profiles are very similar. This indicates that our data set has enough resolving power to discriminate between depth and velocity perturbations at all crustal levels, within estimated model uncertainties.

[23] The horizontally averaged velocity deviations before and after the inversion are shown in Figure 8. By comparing both horizontally averaged deviations, we can see that (1) the reduction of the mean deviation is significant in the three profiles, ranging from >75% in the upper crust to ~50% at the bottom layers and (2) the depth-dependent pattern of the initial mean deviation is not reflected in the final model, which means that the final models depend only slightly on the velocities of the initial ones. Both observations indicate that our final solutions are robust and well constrained by the data set.

[24] We finally performed a checkerboard test to investigate the resolving power of the data set for each profile (Figure 9). A synthetic data set has been calculated for a synthetic velocity model with the same source-receiver geometry as in the real data set. The synthetic model was prepared by adding sinusoidal velocity anomalies with a size of 10 × 5 km in the upper crust and 35 × 12 km in the lower crust and a maximum amplitude of ±7% to the final solution (i.e., the models in Figure 5) (Figure 9). Random noise with the amplitude of the picking errors has been added to the synthetic data set, and the 1-D average model (1-D velocity model with a flat Moho interface) has been calculated for each synthetic data set. The result of the inversion starting from this 1-D average model and the randomized synthetic data set, and the differences with respect to the synthetic model are shown in Figure 9. The pattern of the velocity anomalies is fully recovered, showing only small differences (<2%) within the lower crust. The differences are more significant in profile 3, in agreement

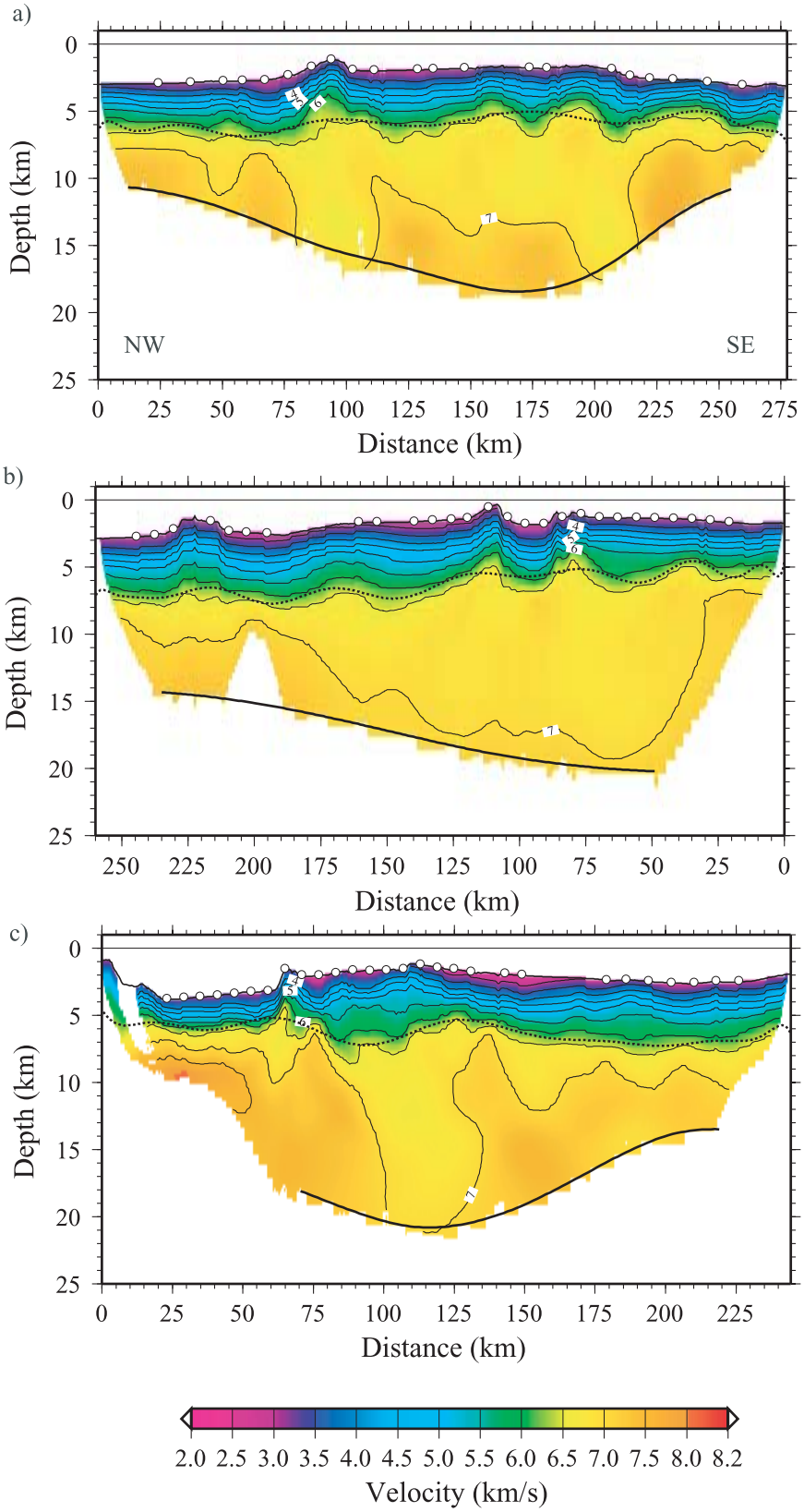

Figure 5. Seismic tomography results. Final averaged velocity models from the 100 Monte Carlo ensembles. (a) Profile 1, southern Cocos, (b) profile 2, northern Cocos, (c) profile 3, Malpelo Ridge. Dashed lines show layer 2/layer 3 interfaces. White circles indicate OBS/OBH locations. Solid circles show instruments displayed in Figure 3.

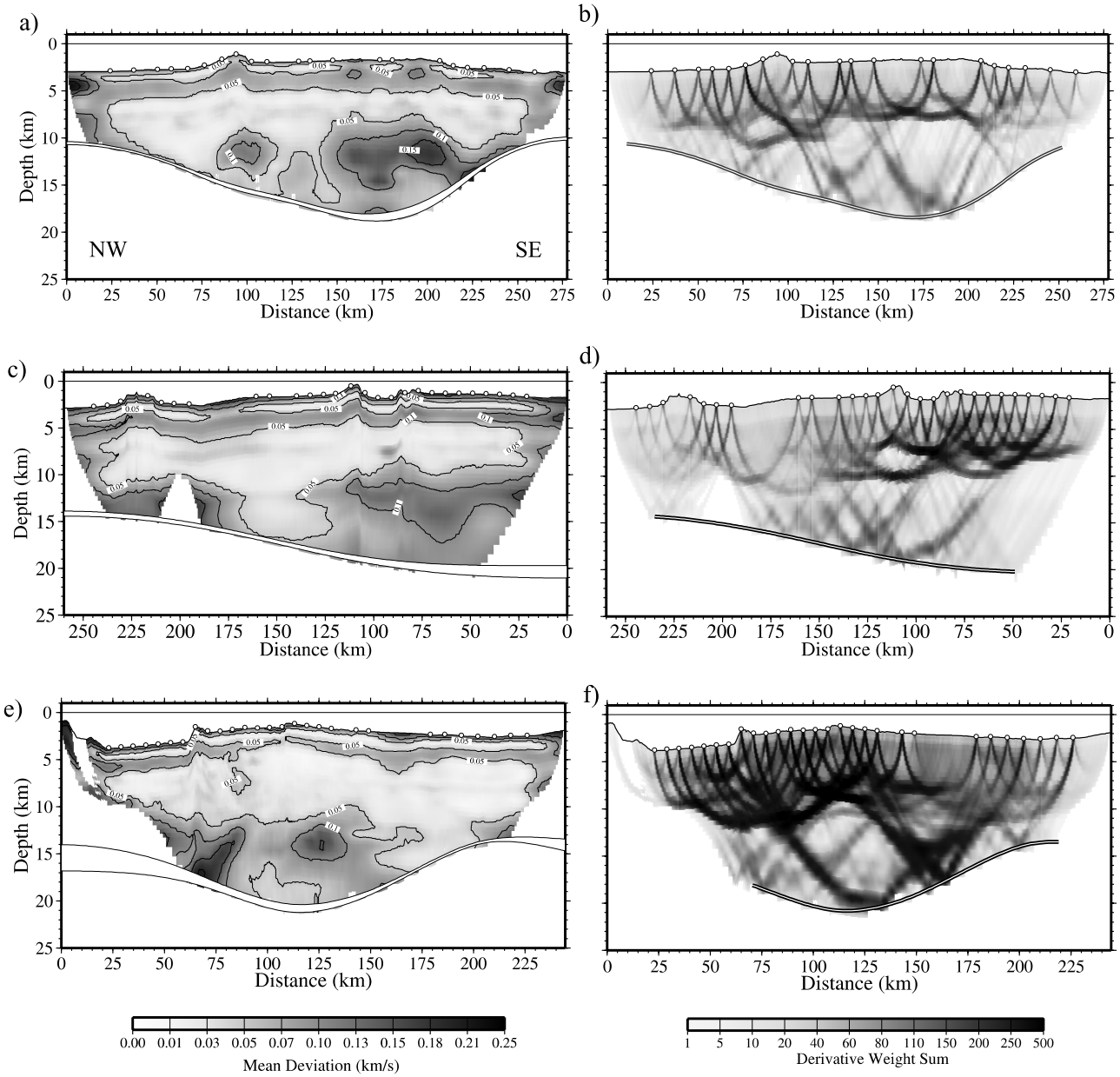

Figure 6. Velocity and Moho depth uncertainties derived from the (left) Monte Carlo analysis and (right) derivative weight sum (DWS) corresponding to the models displayed in Figure 5. (a, b) Profile 1, southern Cocos, (c, d) profile 2, northern Cocos, (e, f) profile 3, Malpelo Ridge.

with the less clear *PmP* phases along this profile. Moreover, the Moho geometry is also recovered successfully, with deviations from the true geometry less than 0.5 km. This suggests again that the velocity-depth ambiguity associated with reflection tomography is insignificant in our study and that the data set has enough spatial resolution with respect to the size of velocity anomalies considered here.

5. Gravity Modeling

[25] In this section, we present gravity modeling for profiles 1 and 3 (Figure 1). Profile 1 is taken as an example to estimate the contribution of the different lithospheric features in the observed gravity anomaly. Since the geometry of the other two experiments and the crustal velocity models are quite similar to this one, we assume that the main conclusions can be generalized to the other two transects. Gravity modeling of profile 3 is done for a different purpose; to constrain the Moho geometry for the NW flank of the transect, which is poorly resolved by seismic tomography.

[26] The goal is to find 2-D density models that can explain the gravity data along the transects and is consistent with the seismic velocity models. Because of the lack of shipboard free-air gravity data, the gravity profiles along both transects have been built using available high-resolution marine gravity data based on satellite altimetry [*Sandwell and Smith*, 1997]. We consider this data set to be sufficient for our analysis, since we are mainly interested in the long-wavelength crustal features. Our gravity calculation is

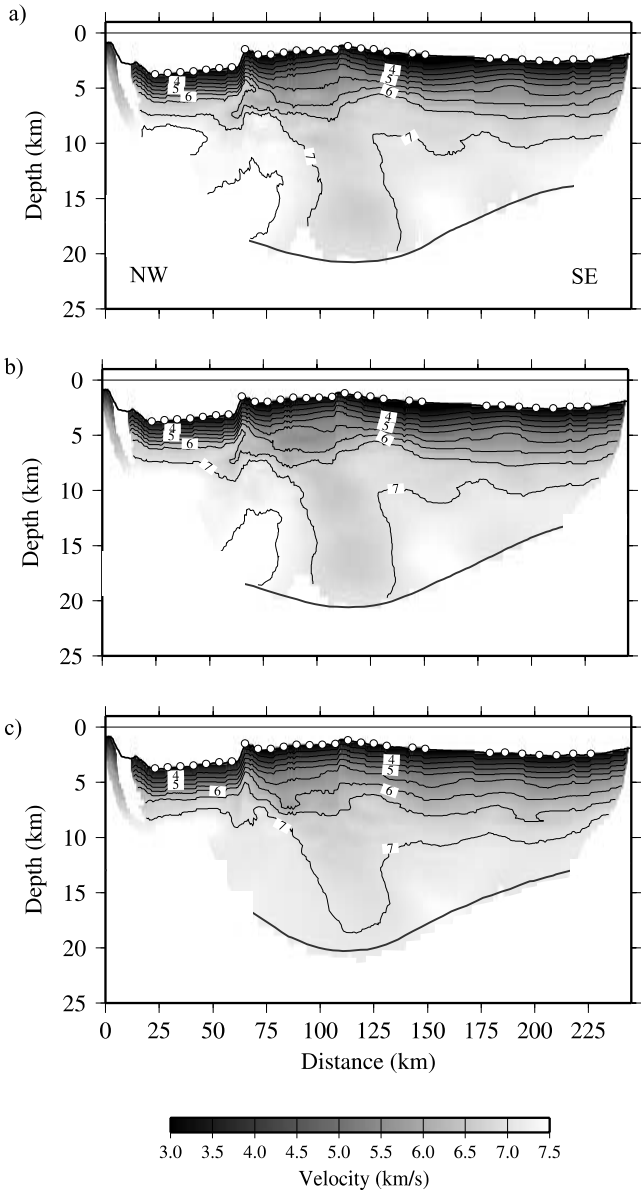

Figure 7. Results of velocity inversion along profile 3 (Figure 1) using the average 1-D model as initial model but different values for the depth kernel weighting parameter w: (a) w = 0.1, (b) w = 1, and (c) w = 10. RMS travel time misfits are 71, 69, and 70 ms, respectively.

based on *Parker*'s [1972] spectral method, which allows calculating the gravity anomaly caused by lateral and vertical density variations (see *Korenaga et al.* [2001] for details).

5.1. Profile 1, Southern Cocos

[27] A significant part of the free-air gravity is caused by seafloor topography and crustal thickness variations. Therefore prior to any attempt to model the crustal (and mantle) density field, it is necessary to correct the gravity anomaly for these two contributions. The topography contribution can be estimated by calculating the gravity signal of the seafloor-water interface and assuming a crustal layer of uniform thickness (7 km) and density (2800 kg/m^3) (Figure 10a). Mantle density is considered to be 3300 kg/m^3. The resulting anomaly is the so-called mantle Bouguer anomaly (MBA) (model a in Figure 10e). This anomaly largely overestimates the observed free-air gravity along the profile, reflecting principally the existence of a thick crustal root beneath the Cocos Ridge.

[28] In the next step, we attempt to correct for the crustal thickness variations (Figure 10b), by incorporating the crust-mantle boundary obtained in the seismic tomography inversion (Figure 5a). The crustal and mantle densities are the same as in model a. The gravity anomaly calculated with this model (model b in Figure 10e) fits better the observed free-air gravity, but there are still differences as large as 40–

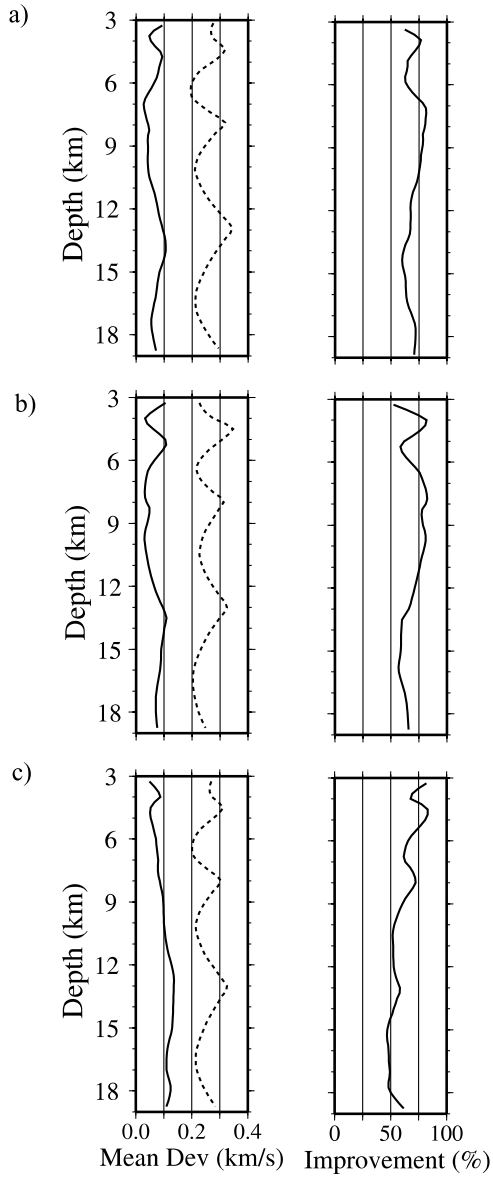

Figure 8. (left) Horizontally averaged velocity deviation from all Monte Carlo ensembles before (solid line) and after (dashed line) the inversion. (right) Relative decreasing, improvement, of the horizontally averaged mean deviation after the inversion. (a) Profile 1, southern Cocos, (b) profile 2, northern Cocos, (c) profile 3, Malpelo Ridge.

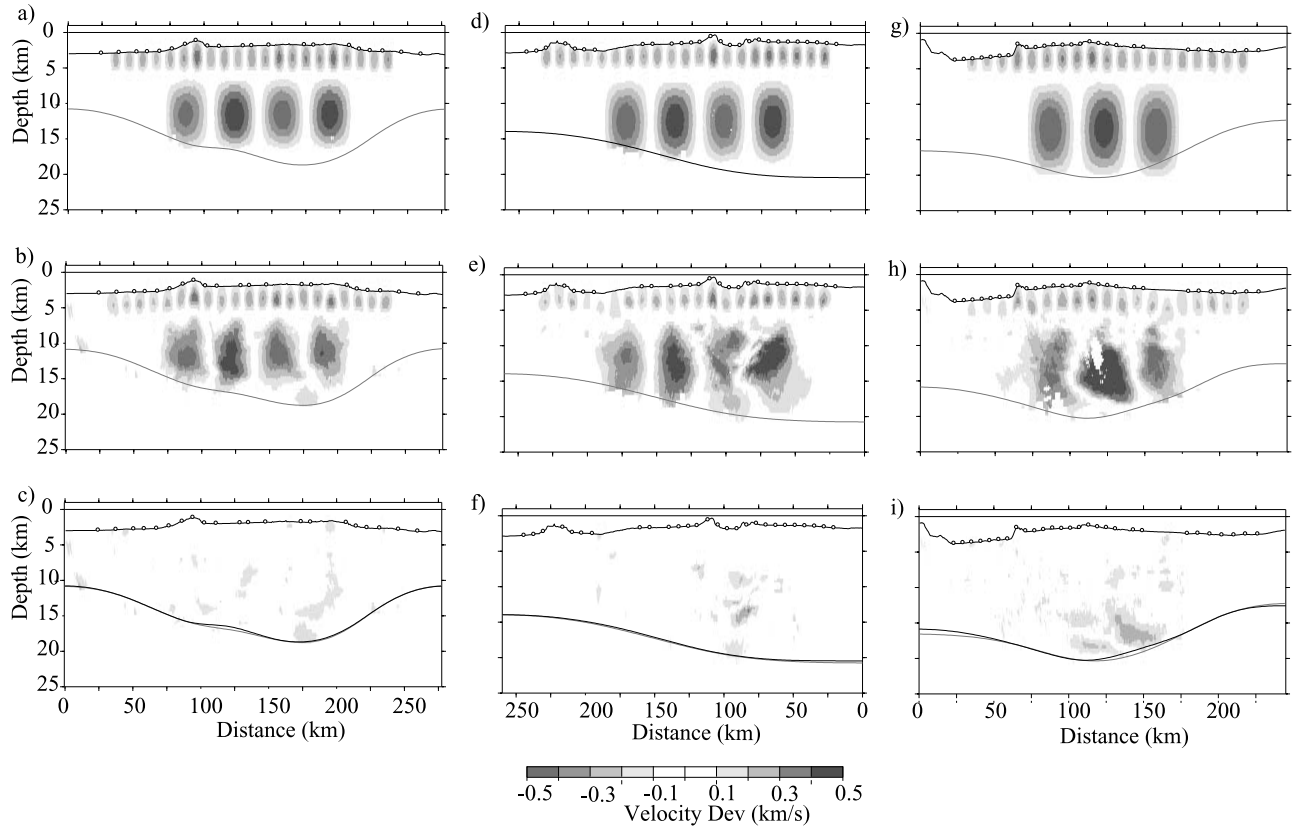

Figure 9. Results of the checkerboard tests. Synthetic models showing (top) the amplitude of velocity anomalies with respect to the background models displayed in Figure 5, (middle) results of tomographic inversion, and (bottom) difference between initial and final models. (a–c) Profile 1, southern Cocos, (d–f) profile 2, northern Cocos, (g–i) profile 3, Malpelo Ridge.

50 mGal in the central part of the ridge. Once corrected for seafloor and Moho topography, the remaining gravity anomaly misfits must reflect crustal and/or mantle density variations with respect to the reference model (model b).

[29] In order to test the influence of the crustal density variations, we have built the third simple model (Figure 10c), which includes crudely the main features observed in the velocity model. This model is composed of two layers with different densities. The upper layer (above 7 km depth) corresponds approximately to our layer 2. Its density is 2600 kg/m^3. The bottom one (below 7 km depth) represents our layer 3, and includes the denser, crustal root. Its density (3000 kg/m^3) is between the density of layer 2 and that of the mantle (3300 kg/m^3). The calculated gravity anomaly (model c in Figure 10e) fits the observed gravity very well, and misfit is smaller than 10–15 mGal along most of the transect. The larger differences (around 90 km and 200 km) are directly associated with the bathymetric highs. These bathymetric features correspond to three-dimensional, seamount-like structures, so the observed gravity differences are most likely due to our assumption of 2-D density structure. This simple model accounts therefore for the long-wavelength gravity anomalies without calling for anomalous mantle densities.

[30] Finally, we have built the fourth model, in which we allowed for lateral and vertical density variations within the crust. The 2-D seismic velocity model (Figure 5a) was directly converted into a crustal density model using empirical velocity-density relations. Because of the lack of seismic reflection data, we employed different conversion rules for each crustal layer only on the basis of the seismic velocities. For velocities lower than 3.2 km/s (approximately sediments) we have used *Hamilton*'s [1978] relation for shale, $\rho = 0.917 + 0.747V_p - 0.08V_p^2$. For velocities between 3.2 and 6.5 km/s (approximately layer 2) we have assumed *Carlson and Herrick*'s [1990] empirical relation, $\rho = 3.61 - 6.0/V_p$, which is based on Deep Sea Drilling Project (DSDP) and Ocean Drilling Program (ODP) core data. Finally, for velocities higher than 6.5 km/s to the crust-mantle boundary (approximately layer 3), we have used *Birch*'s [1961] law for plagioclase, and diabase-gabbro-eclogite, $\rho = 0.375 + 0.375V_p$, which is considered to be more adequate to describe the composition of the oceanic lowermost crust. Mantle density is kept constant (3300 kg/m^3).

[31] All the v-ρ relationships for sediments, layer 2, and layer 3 are calculated at some reference temperature, T, and pressure, P (e.g., 1 GPa, 25°C), and they can be used to calculate the densities from seismic velocities at in situ conditions using estimates of the pressure and temperature partial derivatives [e.g., *Korenaga et al.*, 2001]. The in situ crustal temperatures are calculated using the heat conduc-

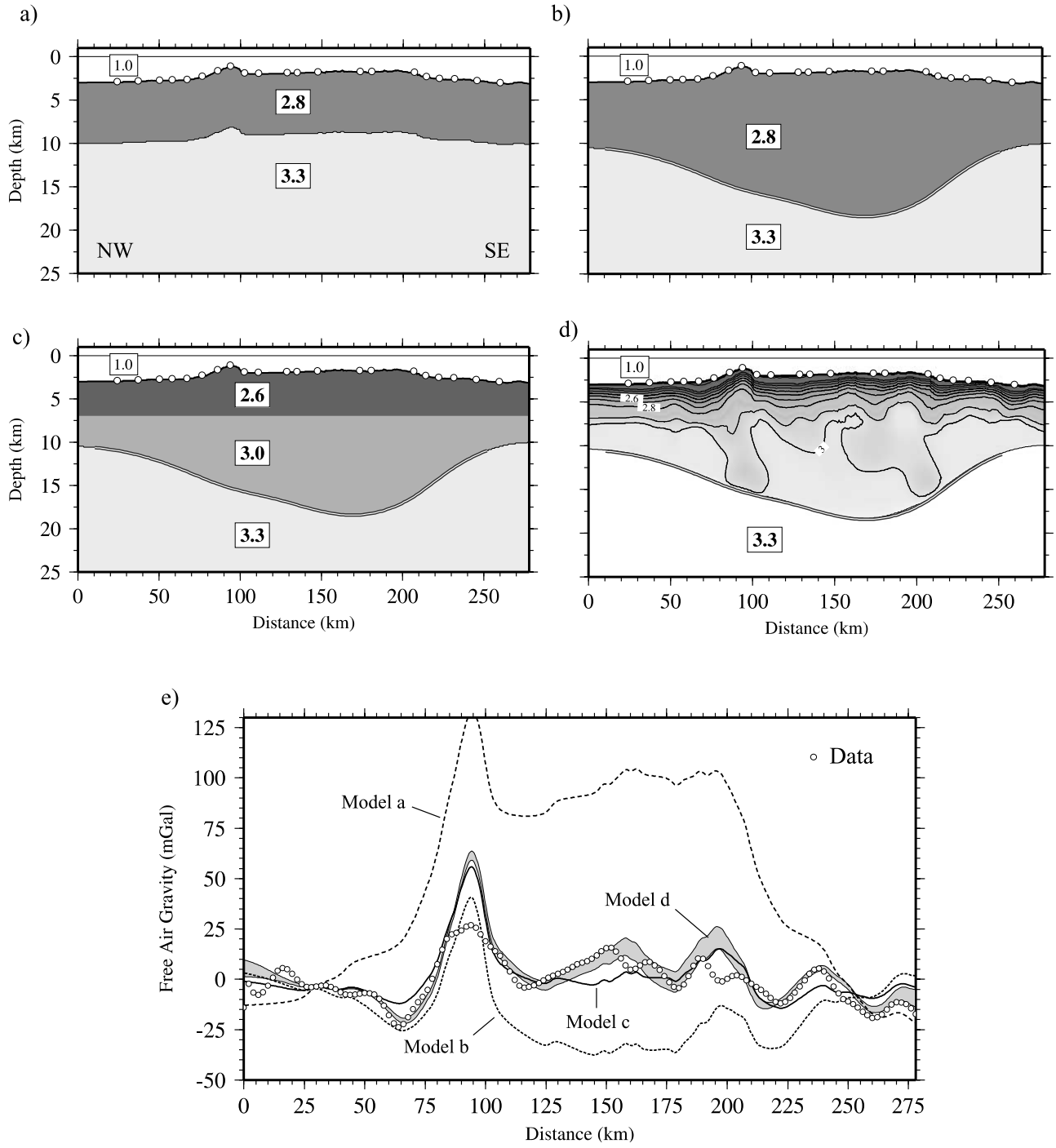

Figure 10. Different density models along profile 1, southern Cocos, corresponding to (a) model a, (b) model b, (c) model c, and (d) model d, described in the text. (e) Observed free-air gravity anomaly (open circles) and calculated gravity anomaly for density models a–d. Shaded zone shows the gravity anomaly uncertainty derived from velocity uncertainty (Figure 6a). RMS misfits are 71, 29, 13, and 5 mGal.

tion equation (1), and the lithostatic pressure is given by equation (2):

$$T(y) = T_0 + \frac{Q_S}{\kappa} y - \frac{\rho H}{2\kappa} y^2 \quad (1)$$

$$P(y) = P_0 + \rho y, \quad (2)$$

where T_0 and P_0 are the temperature and pressure at the surface (assumed to be 0 MPa, 0°C), Q_s is the surficial heat flow, κ is the conductivity (~2.1 W/m °K for gabbro basalt), ρ is the mean density (~2850 kg/m^3 for gabbro basalt), H is the heat production rate, and y is depth.

[32] In oceanic crust, H is very small, and its contribution to the temperature regime is negligible. Q_s is not accurately known at young ocean basins, but it can be inferred using

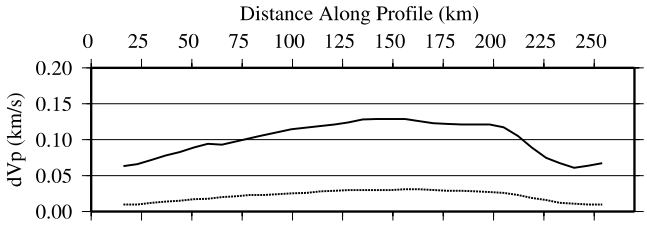

Figure 11. P-T velocity corrections from in situ conditions to the reference state (400°C, 600 MPa) obtained along profile 1, southern Cocos. Solid line corresponds at 100% conductive heat loss and dashed line corresponds at 50% conductive heat loss.

Parsons and Sclater's [1977] empirical law, in which heat flow is applied as a function of the age of the plate, t, $Q_s = 473.02/t^{1/2}$ mW/m^2, for $0 < t < 120$ Ma. Hydrothermal circulation is known to be a significant cooling mechanism for a young oceanic crust [e.g., *Morton and Sleep*, 1985], though it is difficult to quantify its influence. One option is to perform a sensitivity test by comparing velocity corrections for 100% conductive heat loss (no hydrothermal cooling) and for 50% conductive heat loss (Figure 11). Larger *P-T* velocity corrections (up to 0.10–0.15 km/s) correspond to the case without hydrothermal cooling, so we took this value as an upper bound for correction of the in situ crustal velocities.

[33] The 2-D density model along profile 1 obtained after correcting for P-T conditions is shown in Figure 10d. The uncertainty of the velocity model (Figure 6a) is propagated to that of the calculated gravity anomaly on the basis of the 100 Monte Carlo ensembles, though errors associated with the uncertainties of the conversion rules are not considered here (Figure 10e). We can see that the gravity anomaly is fully recovered with misfits smaller than 5–10 mGal along the entire profile, with the only exception at the bathymetric highs. Therefore we can conclude that the seismic velocity model obtained along profile 1 (Figure 5a) is also consistent with the gravity data.

5.2. Profile 3, Malpelo Ridge

[34] As we described earlier, the Moho geometry in the NW flank of profile 3 (0–75 km) is not constrained by *PmP* reflections. Therefore the main purpose of the gravity analysis along this profile is to determine the Moho geometry that best fits the observed gravity anomalies in this part of the transect. To do that, we fixed seismic velocities along the whole profile and the Moho geometry between 75 km and 245 km (Figure 5c), and the model was converted into densities following the same approach as in profile 1 (section 5.1). We used the same empirical conversion laws for the different crustal levels, mantle densities were fixed (3300 kg/m^3), and *P-T* corrections were calculated. Then, we varied the Moho geometry between 0 and 75 km in order to obtain a good fit between observed and calculated gravity anomaly. Finally, uncertainties of the velocity model (Figure 6e) were propagated into that of the gravity anomaly. The final density model is represented in Figure 12a, and the observed and calculated free-air gravity anomalies are shown in Figure 12b. To account for the gravity anomaly, it is necessary to consider a dramatic crustal thinning toward the NW flank of the ridge (Figure 12a). In this part, the crust is only ~6.0 km thick, which is consistent with the shallow mantle-like velocity body in seismic tomography (Figure 5c). Layer 2 is also thinner than in the rest of the transect (~2 km).

6. Discussion

[35] The three profiles investigated in this study are located over seafloor of different ages: ~11 m.y. (profile 1), ~15 m.y. (profile 2), and ~19 m.y. (profile 3). Therefore we must take into account that these structures are the product of the interaction between the Galapagos hot spot and the CNS at three different periods of time. The long-wavelength crustal structure along these profiles provides information on mantle melting process. Thus temporal variations in the relative location of the hot spot and the ridge and/or in the hot spot activity are likely to be reflected by differences in the seismic structure. In this section, we first identify and compare the main features of the velocity structure along the different profiles. Second, the results are used to constrain the range of mantle melting parameters (temperature, upwelling ratio, composition) that can account for the obtained structure, on the basis of mantle melting models [*Korenaga et al.*, 2002]. Third, the significance of the dramatic crustal thinning of the northern flank of Malpelo Ridge is discussed within the geodynamic framework.

6.1. Global Features of the Crustal Structure

[36] The observed long-wavelength crustal structure is similar along the three profiles. In terms of crustal velocities

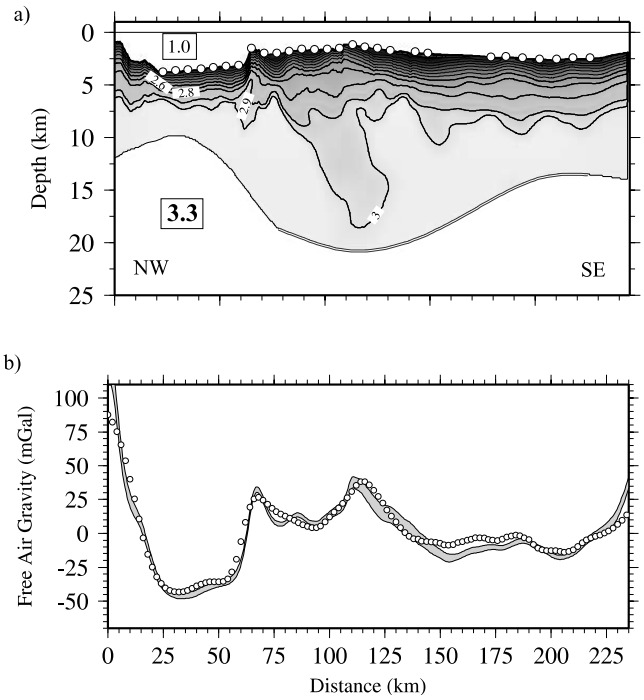

Figure 12. (a) Velocity-derived density model along profile 3, Malpelo Ridge. Densities are in g/cm^3. (b) Observed free-air gravity anomaly (open circles) and calculated gravity anomaly for model a. Shaded zone shows the gravity anomaly uncertainty. RMS misfit is 3.9 mGal.

(Figure 5), the crust can be divided into two internal layers. Layer 2 shows large velocity gradients (2.0 km/s < V_p < 6.5 km/s), in agreement with those described for sediments and the upper igneous crust. Layer 3 displays much more uniform velocities (6.5–7.2 km/s), which are consistent with those described for the oceanic lower crust. It is generally accepted that the velocity gradient within the upper crust (excluding the sediment) is mostly due to changes in rock porosity and alteration, which do not affect strongly the lower crust [*Detrick et al.*, 1994]. This is consistent with the two following observations:

[37] First, almost no seismic reflections coming from the layer 2/3 boundary have been identified in the seismic records, which suggests that this interface does not represent a first-order discontinuity between two lithologically different layers, but it represents more likely a transition zone between the upper, altered, layer and the lower, unaltered, layer. In contrast, other results from seismic studies in the East Pacific Rise [e.g., *Harding et al.*, 1989] show that the layer 2/3 transition (~6.5 km/s) coincides with the depth of the magma chamber, which suggests that the change in velocity gradient may reflect a change in primary rock type from basaltic to gabbroic crust. However, it is also likely that the change in velocity gradient from alteration and the change in velocity gradient from rock type are casually related.

[38] Second, the long-wavelength thickness of layer 2 is quite uniform along all transects (3.5 ± 0.5 km) regardless of total crustal thickness variations (which can be as much as 11–12 km between several parts of the seismic profiles). Therefore the amount of layer 2 extrusives seems to be independent of the amount of melting generated at the spreading center, which means that crust must grow dominantly through plutonic, rather than extrusive, processes. This observation could easily be explained if the velocity increase within layer 2 is mainly by crack closure due to lithostatic pressure [*Bratt and Purdy*, 1984]. This implies that at ~3–4 km below seafloor cracks are mostly closed, and thus that the uniform velocity of layer 3 reflect essentially the bulk composition of the igneous crust. This hypothesis can also explain qualitatively why crustal overthickening is mainly accommodated in oceanic layer 3 [e.g., *Mutter and Mutter*, 1993]. Similar results have been obtained across the Cocos Ridge [*Walther*, 2002] (profile 1 in Figure 1) and Malpelo Ridge [*Trummer et al.*, 2002] (profile 3 in Figure 1) using forward modeling techniques.

[39] The maximum crustal thickness along the three transects varies between 16.5 km (profile 1) and 18.5–19.0 km (profiles 2 and 3). These observations indicate that the amount of melting generated beneath the spreading center decreased between ~20 Ma (profile 3) and ~11 Ma (profile 1), suggesting that the plume intensity have decayed between 20 and 11 Ma. However, it is difficult to infer whether this decay is related with absolute variations in the hot spot activity (e.g., temperature variations), or with variations on the relative location of the hot spot with respect to the spreading center. A recent geodynamic reconstruction of the GVP in the basis of crustal thickness estimations of the Cocos, Malpelo and Carnegie Ridges indicates that isochronous differences of crustal thickness at both sides of the spreading center can be well explained by relative variations on the hot spot-ridge location [*Sallarès and Charvis*, 2003].

[40] Another striking feature observed along all three transects is that mean layer 3 velocities (i.e., the bulk velocities of the igneous crust) tend to be lower where the crust is thicker, showing an overall anticorrelation between mean layer 3 velocities and total crustal thickness (Figure 13). This anticorrelation was not observed in the previous forward velocity models obtained across Cocos and Malpelo Ridges [*Trummer et al.*, 2002; *Walther*, 2002]. Unlike our study, however, their velocity models have been obtained by trial and error. In addition, uncertainty analysis and estimation velocity-depth ambiguities are lacking in these studies, making difficult to ascertain how well constrained are the lower crustal velocities and the Moho geometry. Also, it is essential to know the velocity uncertainty and the degree of velocity-depth ambiguities in order to relate crustal velocity with melting processes. Since lower crustal velocities are supposed to reflect the bulk crustal composition, any melting model trying to explain the origin of the overthickened oceanic crust must explain this overall anticorrelation. This is discussed in section 6.2.

6.2. Melting Parameters and Hot Spot-Ridge Interaction

[41] It is widely accepted that new oceanic crust is formed by decompressional melting of mantle upwelling beneath diverging plates at a spreading center [e.g., *McKenzie and Bickle*, 1988]. Basic assumptions usually made include the following: (1) mantle upwelling is plate driven (passive), (2) mantle source composition is homogeneous (approximately pyrolite), and (3) all mantle melt is emplaced as seismically observable igneous crust. Therefore, if all these assumptions are valid, the amount of melting (and the crustal thickness and composition) would be essentially a function of the mantle temperature. *White et al.* [1992] used this idea to develop a method to estimate the range of mantle temperatures that can account for seismic crustal thickness and basalt geochemistry.

[42] Following this method, *White and McKenzie* [1995] showed that for a plume lying beneath a spreading center (Iceland), mantle potential temperatures of ~1500°C are required to explain crustal thickness and basalt geochemistry, which is about 150°C higher than required to generate normal MORB and ~7 km thick crust (~1350°C). These results are quite consistent with those obtained in the GVP, where excess temperatures of 50°–150°C were inferred from gravity analysis along the present and paleoaxes of the Cocos-Nazca Spreading Center [*Ito and Lin*, 1995]. The variations in axial temperatures were attributed to temporal variations in the distance between the hot spot and the migrating ridge. Slightly higher excess temperatures (~200°) were obtained by comparing along-axis gradients in the strength of OIB signatures with topography [*Schilling*, 1991]. Similar to *White and McKenzie* [1989], these studies also assumed that plume buoyancy and crustal thickening are entirely of thermal origin.

[43] Another conclusion of *McKenzie and Bickle*'s [1988] work is that not only crustal thickness, but also crustal seismic velocity, is sensitive to mantle potential temperature. These authors showed that infinite lithospheric stretch-

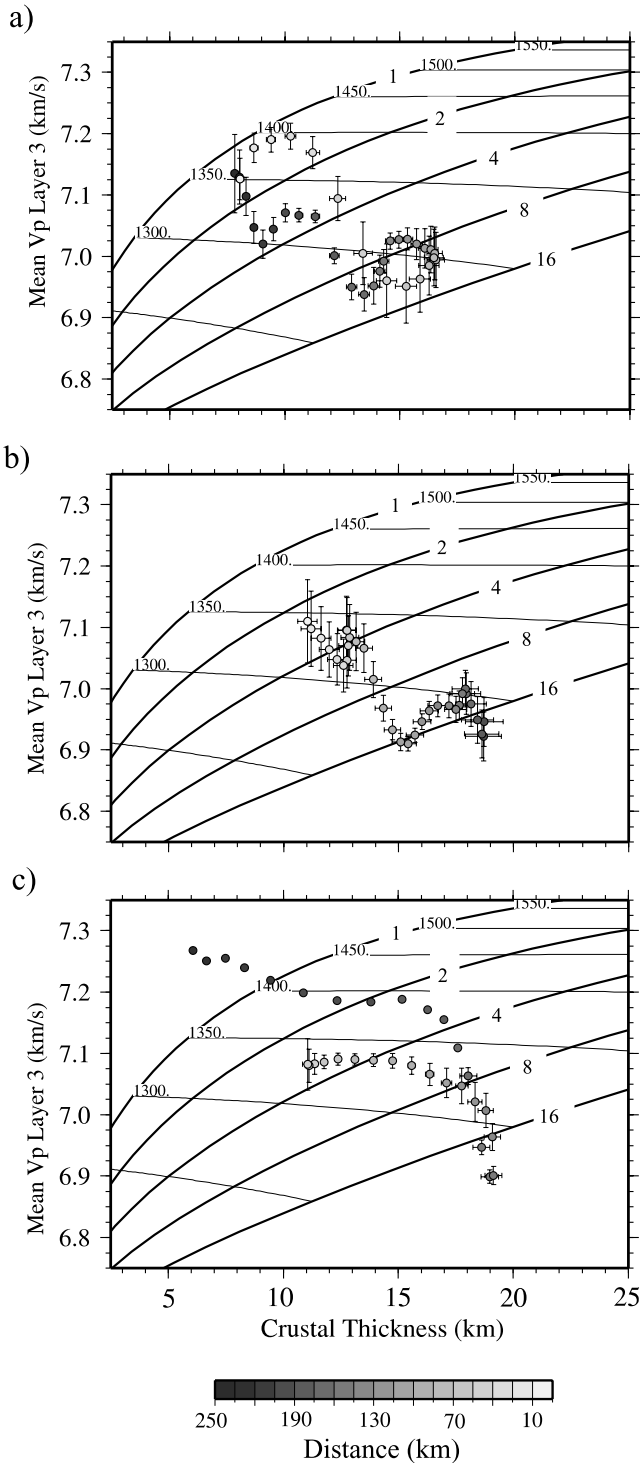

Figure 13. Standard H-V_p diagrams. Corrected mean layer 3 velocity and crustal thickness within a 25 km wide moving window (circles with error bars) are compared with mantle potential temperatures (thin lines) for different upwelling rates (thick lines). Diagrams are derived from the mantle melting models of *Korenaga et al.* [2002]. The reference state is 400°C, 600 MPa, and the mantle composition is pyrolitic. (a) Profile 1, southern Cocos, (b) profile 2, northern Cocos, (c) profile 3, Malpelo Ridge.

ing over normal temperature mantle produces melt with a MORB-like composition. As potential temperature rises above normal, the MgO content of melt increases progressively. Since the elastic properties of igneous rocks are known to be sensitive to the MgO content [e.g., *Kelemen and Holbrook*, 1995], if all MgO-rich melt is emplaced as seismically observable crust (i.e., there is no subcrustal fractionation), the seismic velocity of igneous crust would also have to increase systematically. *White and McKenzie* [1989] showed that if mantle temperature is increased by about 200°C above normal, the mean velocity of igneous crust would increase by as much as 0.2–0.3 km/s. Therefore, if the initial assumptions were valid and the estimations of excess temperatures associated with the presence of the hot spot (150°–200°C) were also correct, we would have to obtain higher seismic velocities within the thickened lower crust (affected by the hot spot). Similar interpretations have been widely invoked to account for the origin of the thick crust and high lower crustal velocities generally observed in passive volcanic margins [e.g., *Morgan et al.*, 1989; *Kelemen and Holbrook*, 1995], oceanic plateaus [e.g., *Charvis et al.*, 1995; *Charvis and Operto*, 1999], and aseismic volcanic ridges [e.g., *Grevemeyer et al.*, 2001a, 2001b].

[44] Our results for the GVP show the contrary to this prediction. Seismic velocities tend to be lower where the crust is thicker, and the uncertainty in mean layer 3 velocity is sufficiently small to conclude that the observed trend is real and not an inversion artifact. Therefore some of the initial *McKenzie and Bickle*'s [1988] assumptions need to be revisited for the interpretation of our velocity models.

6.2.1. Passive Versus Active Upwelling

[45] Several numerical studies have shown that the influence of active (plume-driven) upwelling beneath spreading centers can be significant in the presence of mantle plumes [*Ribe*, 1996; *Ito et al.*, 1996]. The important role of the active upwelling in the generation of the North Atlantic igneous province has been pointed out recently by two different geophysical and geochemical studies. *Korenaga et al.* [2002] developed a new method in which a quantitative relation between sesimic parameters (crustal thickness, H, and bulk lower crustal velocity, V_p) and mantle melting parameters (mantle potential temperatures, T, and active upwelling ratio, χ) is established on the basis of data from a number of mantle melting experiments, assuming an homogeneous, pyrolitic composition for the mantle source. A thorough discussion on the method used to establish a general relation between the bulk crustal velocity and the lower crustal velocity of igneous crust, as well as an estimation of the uncertainty bounds of the relationships derived from experimental data is given by *Korenaga et al.* [2002]. The standard deviation of the regression of compressional wave velocity for different pressures and fractions of melting based on the results of mantle melting experiments is only 0.05 km/s. By comparing the calculated H-V_p diagrams with the results of a wide-angle seismic experiment in the Greenland margin, they also concluded that the seismic structure of the margin is not the result of anomalously high mantle temperatures, but mostly the result of vigorous upwelling of a normal temperature mantle. *Maclennan et al.* [2001] showed that in central Iceland, the geochemical signatures and observed crustal thickness

cannot be simultaneously reproduced using a purely passive upwelling model. It is possible, however, to explain both observations if mantle potential temperatures are high (~1500° C, as estimated by *White and McKenzie* [1995]) but melting rates in the deepest part of the melting zone (>100 km depth) are about 10 times higher than those expected from plate-driven upwelling alone.

[46] In order to test these hypotheses with our results, we have used the standard H-V_p diagrams of *Korenaga et al.* [2002], in which a range of expected seismic parameters (H, V_p) are represented as a function of T and χ (Figure 13). The long-wavelength structure is obtained by calculating H and V_p within a 25 km wide moving window. Since only layer 3 velocities are likely to reflect the bulk composition of the igneous crust, V_p is calculated only for this part of the crust (i.e., from the layer 2/3 boundary to the Moho). Uncertainties of velocity and Moho depth parameters obtained along the transects (Figure 6) are used to place error bounds for H and V_p. Since standard H-V_p diagrams are calculated at particular P-T conditions (400°C, 600 MPa), it is necessary to correct V_p from the in situ conditions to this reference state, following the approach that we described in section 5.1. The corrected results along all profiles are shown in Figure 13.

[47] The basic interpretation of the results seems to be straightforward: if mantle source is homogeneous and all melt is emplaced as crust, the observed seismic velocity and the crustal thickness of the thickened ridge's crust have to be explained by vigorous upwelling ($\chi > 16$) of colder than normal mantle ($T < 1300$°C). In contrast, results in the normal oceanic basins (i.e., at both limits of profile 1, Figure 13a) are consistent with passive upwelling ($\chi \sim 1$) of normal temperature mantle ($T \sim 1350$°C). The only exception to the general trend is the NW flank of the Malpelo Ridge (Figure 13c), in which crust is thinner and mean V_p is higher than in the rest of the profiles (see discussion in section 6.3). It is clear, however, that our seismic observations contradict directly with the original hot spot hypothesis, so it is necessary to consider the validity of the other assumptions.

6.2.2. Subcrustal Fractionation and Mantle Source Heterogeneities

[48] The other two basic assumptions of all mantle melting models are that (1) all melt is emplaced as seismically observable igneous crust and (2) mantle source composition is homogeneous. In this section, we discuss how subcrustal fractionation and the presence of source heterogeneities could affect the melting process and, in turn, the observed seismic parameters.

[49] Regarding the first assumption, if there are actually missing subcrustal components composed of high-velocity minerals (e.g., olivine, clinopyroxene), the seismic velocities of the resulting lower igneous crust could become lower than those expected for crystallization of a primary, mantle-derived melt. Recent results of fractional crystallization modeling at high pressures [*Korenaga et al.*, 2002] showed that the effect of subcrustal fractionation is significant only for high lower crustal velocities (as much as 0.2 km/s for a 7.6 km/s mineral assemblage). For low layer 3 velocities as those observed in the Cocos and Malpelo Ridge ($V_p <$ 7.0 km/s), however, the effect is less than 0.05 km/s even for 30% subcrustal fractionation. Therefore the main effect of a missing subcrustal component would be basically an underestimation of the total amount of melting, but without significant influence on the range of possible mantle potential temperatures. If there is subcrustal fractionation in the GVP, the real upwelling ratio would have to be even higher to that estimated with the standard H-V_p diagram.

[50] Regarding the second assumption, it is generally assumed that the upper oceanic mantle is composed of relatively dry pyrolite, since the composition of most oceanic peridotites corresponds well with that expected from melting of a pyrolitic mantle. Within this general framework, the local variations observed in crustal thickness, composition and physical properties of the igneous oceanic crust (e.g., in oceanic plateaus, aseismic ridges, volcanic margins) have been mostly attributed to thermal anomalies of the mantle source, and not to compositional anomalies, in accordance with the original hot spot hypothesis. In the GVP, for example, the excess temperatures associated with the presence of the Galapagos hot spot have been estimated mainly from gravity analysis along the Cocos-Nazca Spreading Center [*Schilling et al.*, 1991; *Ito and Lin*, 1995; *Canales et al.*, 1997, 2002]. All these studies relate misfits between the observed free-air gravity anomaly and the calculated anomaly for a constant-density crustal layer with density anomalies in the shallow upper mantle, which in turn are associated with thermal anomalies. However, as we have shown in section 5.1, a thorough calculation of the crustal densities along our transects can account for the observed gravity without considering anomalous densities (temperatures) in the mantle (Figure 10). An alternative explanation is that thermal/density anomalies are irrelevant given that all our profiles are away from zero age.

[51] Basalt samples in a number of hot spots including Hawaii [*Hauri*, 1996], Açores [*Schilling et al.*, 1983], Iceland [*Korenaga and Kelemen*, 2000], and Galapagos [*Schilling et al.*, 1982; *Detrick et al.*, 2002] show striking geochemical anomalies in incompatible and major elements with respect to MORB. Though the concentration of these elements is also strongly influenced by the process of melting itself [*Langmuir et al.*, 1992], the existence of such anomalies is generally considered to indicate the presence of compositional heterogeneities in the mantle source. A recent study in the GVP showed that lavas erupted along the axis of the CNS show increased concentrations of incompatible elements (H_2O, Na, Ca, Al) as the Galapagos hot spot is approached from the west [*Detrick et al.*, 2002]. Since incompatible elements tend to be more abundant in melts formed by low-degree melting, the authors concluded that part of the melting beneath the most plume-influenced segment of the ridge represents melting from a large region of hydrous (or incompatible element) enriched mantle. By depressing the solidus, an hydrous root in the mantle source would allow larger amounts of melting than a dry source for a given mantle potential temperature [*Plank and Langmuir*, 1992], and thus it could explain qualitatively the crustal overthickening with lower active upwelling rates. However, the extent of partial melting within the hydrous root is likely to be low [*Hirth and Kohlstedt*, 1996; *Braun et al.*, 2000], so it seems difficult to explain all crustal overthickening (up to >10 km) by this process alone. Another possibility to be considered is the coupling of hydrous melting with active

upwelling at the base of the mantle melting zone. *Ito et al.* [1999] and *Maclennan et al.* [2001] suggested that this is the case of the Icelandic plume. Coupling of hydrous melting and active upwelling could potentially account for the crustal overthickening, but it is less evident to understand if it can account also for the low velocities. On the basis of the relationship between V_p and the mean fraction (F) and pressure (P) of melting derived by *Korenaga et al.* [2002] from mantle melting experiments, it is not easy to see if melts generated at low F and high P should display higher or lower seismic velocity than those generated at high F and low P. It is therefore necessary to perform further mantle melting modeling including deep damp melting in order to investigate if it is a plausible process to explain the anticorrelation between crustal thickness and seismic velocity.

[52] As an alternative explanation, we consider a more drastic, major element heterogeneity in the mantle source. A geochemical study based on major and trace element chemistry of high-MgO lavas sampled within the North Atlantic igneous province suggested that this province is characterized by significant major element source heterogeneity possibly resulting from basalt addition prior to melting [*Korenaga and Kelemen*, 2000]. In particular, they suggest that primary melts must be produced by a mantle source enriched in iron (Mg # < 0.87) as compared with the pyrolitic MORB source (Mg # ~0.90). Subsequently, *Korenaga et al.* [2002] showed that having such a fertile mantle source would reduce the apparent upwelling ratio by a factor of 3–5 in comparison to the melting of a pyrolitic source. In addition, the elastic properties of igneous rocks are sensitive to the Mg #. High concentrations of Mg with respect to Fe tend to increase significantly bulk seismic velocities of the igneous residue [e.g., *Bass*, 1995]. In the GVP, lavas erupted along axis show systematically lower Mg # in the most hot spot-influenced region than in the distal segments [*Detrick et al.*, 2002]. These authors associated the anomaly in the Mg # to differences in the crystal fractionation processes related with the observed depth variations of the magma chamber. We suggest, however, that it may also reflect the existence of a local Fe-rich mantle source anomaly, similar to what has been described for the North Atlantic igneous province. This could explain qualitatively why lower crustal velocities of Cocos and Malpelo Ridges are lower than those expected for a crust generated by melting of a homogeneous pyrolitic mantle. However, our limited understanding of melting of a non-pyrolitic mantle prevents to perform a comprehensive analysis of such a process.

6.3. Rifting of the Malpelo Ridge?

[53] The joint interpretation of seismic and gravity data along profile 3 constrain the crustal structure across the Malpelo Ridge (Figures 6c and 12a). As we stated in the previous section, the seismic structure obtained in the SE part of the transect (between 75 and 245 km along profile) is quite similar to that obtained along the other two profiles, showing uniform layer 2 thickness, a well-developed crust-mantle boundary, a gradual crustal thinning, and a mean layer 3 velocity increasing as we approach the oceanic basin. The northern flank of the ridge (0–75 km along profile), however, shows a different behavior. First, layer 2 is quite thinner than in the rest of the profile. Second, the Moho interface does not seem to be well developed, since *PmP* reflections are lacking in this part of the transect. Third, the transition between the crest of the ridge and the thinned crust is very sharp (almost 10 km of crustal thinning in less than 50 km) (Figure 12a). Moreover, bathymetry shows a very prominent scarp in the same segment. Finally, mean lower crustal velocities (7.2–7.3 km/s) are significantly higher than in the other profiles (Figure 13).

[54] These notable differences between the crustal structure of the northern flank of Malpelo Ridge and the rest of the transects suggest that the mechanism of generation and the geodynamical evolution of this part of the ridge must be different to what we described in section 7.2 for the origin of the aseismic ridges. On the basis of our observations, we suggest that Malpelo and Regina Ridge were separated by the differential motion along the present-day axis of the Coiba transform fault (Figure 2). This division probably took place after the opening of the PFZ. This hypothesis was already suggested by *Lonsdale and Klitgord* [1978] on the basis of the seafloor morphology and by *Marcaillou et al.* [2001] on the basis of seismic data, but further evidence was lacking.

[55] A plausible tectonic scenario would be the following. The thickened Malpelo and Carnegie Ridges were formed by the interaction between the ridge and the hot spot at about 20 Ma. Then, Cocos and Carnegie separated from each another by continuous seafloor spreading in the CNS between 20 and 9 Ma. At this time, subduction of eastern Cocos plate beneath Middle America blocked, triggering the opening of the PFZ and the subsequent separation of the Malpelo and Cocos Ridge [*Sallarès and Charvis*, 2003]. Similarly, the subduction of northeasternmost Cocos plate beneath northern Colombia probably blocked later on, leading to the opening of the E-W trending Coiba transform fault and the separation of Regina and Malpelo Ridges.

7. Conclusions

[56] We have investigated the seismic and density structure of the Cocos and Malpelo Volcanic Ridges, which are the result of the interaction between the Galapagos melt anomaly and the Cocos-Nazca spreading center during the last 20 m.y. A joint refraction/reflection travel time inversion method was employed to constrain the seismic velocity field. The uncertainty of the model parameters has been estimated with Monte Carlo analysis. Density models have been derived from the velocity models using standard velocity-density conversion laws.

[57] Our results show that the maximum crustal thickness along these profiles ranges between 16.5 km (southern Cocos) and 18.5–19.0 km (northern Cocos and Malpelo). The crustal structure shows an upper layer characterized by high velocity gradients (layer 2) and a lower layer with nearly uniform velocity (layer 3). Layer 2 thickness is quite uniform along all transects regardless of total crustal thickness variations; crustal overthickening is mainly accommodated by layer 3. This suggests that velocity increase within layer 2 is basically an effect of crack closure due to lithostatic pressure, and then layer 2/3 boundary is interpreted as the bottom limit of the transition zone between the upper, altered, crustal part and the lower, unaltered, one.

[58] Furthermore, our results also show an overall anticorrelation between crustal thickness and bulk lower crustal velocities, which is the contrary to the prediction of the plume hypothesis. The interpretation of our velocity models, in conjunction with mantle melting models as well as other geophysical and geochemical data, indicates that assumptions of the thermal plume hypothesis may not be valid for the Galapagos melt anomaly. We suggest that both the seismic structure and the geochemical observations could be better explained if mantle melting were dominated by moderate to vigorous upwelling of mantle with normal temperature but with an anomalous major element composition.

[59] The NW limit of the Malpelo Ridge shows a dramatic crustal thinning, and displays high lower crustal velocities and a poorly defined crust-mantle boundary, suggesting that the original Malpelo Ridge was separated between current Malpelo and Regina Ridges after the initiation of the motion along the Coiba transform fault.

[60] **Acknowledgments.** We thank Jun Korenaga for his help with the tomography and gravity codes and for his thorough and constructive revision of the original version of the manuscript. We also thank Timothy Henstock, Satish Singh, and the Associate Editor for their comments and suggestions. We acknowledge the captain of the R/V *Sonne*, Henning Pepenhagen, the ship's crew, and all the scientific staff that participated in the PAGANINI-1999 experiment. The PAGANINI *Sonne* cruise (SO-144) was financed by the German Ministry for Education and Research (BMBF) under grant 03G144A, and the French participation in the project was additionally funded by the EU Program "Training and Mobility of Researchers," Access to Large Scale Facilities, project: ERBFMGECT 950025. V. Sallarès was financially supported during the development of the work by a grant from the EU Marie Curie postdoctoral fellowship, under contract HPMF-CT-1999-00397. One of his visits to Geomar was also supported by the EU Program "Improving Human Potential," Access to Research Infrastructure, project: HPRI-CT-1999-00037.

References

Barckhausen, U., C. R. Ranero, R. von Huene, S. C. Cande, and H. A. Roeser, Revised tectonic boundaries in the Cocos plate off Costa Rica: Implications for the segmentation of the convergent margin and for plate tectonic models, *J. Geophys. Res.*, *106*, 19,207–19,220, 2001.

Bass, J. D., Elasticity of minerals, glasses, and melts, in *Mineral Physics and Crystallography: A Handbook of Physical Constants*, *AGU Ref. Shelf*, vol. 2, edited by T. J. Ahern, pp. 45–63, AGU, Washington D.C., 1995.

Bickel, S. H., Velocity-depth ambiguity of reflection traveltimes, *Geophysics*, *55*, 266–276, 1990.

Birch, F., The velocity of compressional waves in rocks to 10 kilobars, part 2, *J. Geophys. Res.*, *66*, 2199–2224, 1961.

Bratt, S. R., and G. M. Purdy, Structure and variability of oceanic crust in the flanks of the East Pacific Rise between 11° and 13°N, *J. Geophys. Res.*, *89*, 6111–6125, 1984.

Braun, M. G., G. Hirth, and E. M. Parmentier, The effects of deep damp melting on mantle flow and melt generation beneath mid-oceanic ridges, *Earth Planet. Sci. Lett.*, *176*, 339–356, 2000.

Canales, J. P., J. J. Dañobeitia, R. S. Detrick, E. E. E. Hooft, R. Bartolomé, and D. R. Naar, Variations in axial morphology along the Galapagos spreading center and the influence of the Galapagos hotspot, *J. Geophys. Res.*, *102*, 27,341–27,354, 1997.

Canales, J. P., G. Ito, R. S. Detrick, and J. Sinton, Crustal thickness along the western Galapagos spreading center and compensation of the Galapagos hotspot swell, Earth planet, *Sci. Lett., Earth Planet. Sci. Lett.*, *203*, 311–327, 2002.

Carlson, R. L., and C. N. Herrick, Densities and porosities in the oceanic crust and their variations with depth and age, *J. Geophys. Res.*, *95*, 9153–9170, 1990.

Charvis, P., and S. Operto, Structure of the Cretaceous Kerguelen Volcanic Province (southern Indian Ocean) from wide-angle seismic data, *J. Geodyn.*, *28*, 51–71, 1999.

Charvis, P., M. Recq, S. Operto, and D. Brefort, Deep structure of the northern Kerguelen Plateau and hotspot-related activity, *Geophys. J. Int.*, *122*, 899–924, 1995.

DeMets, C., R. G. Gordon, D. F. Argus, and S. Stein, Current plate motions, *Geophys. J. Int.*, *101*, 425–478, 1990.

Detrick, R. S., J. Collins, R. Stephen, and S. Swift, In situ evidence for the nature of the layer 2/3 boundary in oceanic crust, *Nature*, *370*, 288–290, 1994.

Detrick, R. S., J. M. Sinton, G. Ito, J. P. Canales, M. Behn, T. Blacic, B. Cushman, J. E. Dixon, D. W. Graham, and J. J. Mahoney, Correlated geophysical, geochemical, and volcanological manifestations of plume-ridge interaction along the Galápagos Spreading Center, *Geochem. Geophys. Geosyst.*, *3*(10), 8501, doi:10.1029/2002GC000350, 2002.

Grevemeyer, I., E. R. Flueh, C. Reichert, J. Bialas, D. Klaeschen, and C. Kopp, Crustal architecture and deep structure of the Ninetyeast Ridge hotspot trail from active source ocean bottom seismology, *Geophys. J. Int.*, *144*, 1–22, 2001a.

Grevemeyer, I., W. Weigel, S. Schussler, and F. Avedik, Crustal and upper mantle seismic structure and lithospheric flexure along the Society Island hotspot chain, *Geophys. J. Int.*, *147*, 123–140, 2001b.

Hamilton, E. L., Sound velocity-density relations in seafloor sediments and rocks, *J. Acoust. Soc. Am.*, *63*, 366–377, 1978.

Harding, A. J., J. A. Orcutt, M. E. Kappus, E. E. Vera, J. C. Mutter, P. Buhl, R. S. Detrick, and T. M. Brocher, The structure of young oceanic crust at 13°N on the East Pacific Rise from expanding spread profiles, *J. Geophys. Res.*, *94*, 12,163–12,196, 1989.

Harpp, K. S., and W. M. White, Tracing a mantle plume: Isotopic and trace element variations of Galapagos seamounts, *Geochem. Geophys. Geosyst.*, *2*, Paper 2000GC000137, 2001.

Hauri, E. H., Major-element variability in the Hawaiian mantle plume, *Nature*, *382*, 415–419, 1996.

Hey, R., Tectonic evolution of the Cocos-Nazca spreading center, *Geol. Soc. Am. Bull.*, *88*, 1404–1420, 1977.

Hirth, G., and D. L. Kohlstedt, Water in the oceanic upper mantle: Implications for rheology, melt extraction and the evolution of the lithosphere, *Earth Planet. Sci. Lett.*, *144*, 93–108, 1996.

Hoernle, K. A., R. Werner, J. Phipps-Morgan, J. Bryce, and J. Mrazek, Existence of complex spatial zonation in the Galapagos plume for at least 14. 5 Ma, *Geology*, *28*, 435–438, 2000.

Ito, G., and J. Lin, Oceanic speading center hotspot interactions-constraints from along-isochron bathymetric and gravity anomalies, *Geology*, *23*, 657–660, 1995.

Ito, G., J. Lin, and C. W. Gable, Dynamics of mantle flow and melting at a ridge-centered hotspot: Iceland and the Mid-Atlantic Ridge, *Earth Planet. Sci. Lett.*, *144*, 53–74, 1996.

Ito, G., Y. Shen, G. Hirth, and C. J. Wolfe, Mantle flow, melting and dehydration of the Iceland mantle plume, *Earth Planet. Sci. Lett.*, *165*, 81–96, 1999.

Kelemen, P. B., and W. S. Holbrook, Origin of thick, high-velocity igneous crust along the U.S. East Coast margin, *J. Geophys. Res.*, *100*, 10,077–10,094, 1995.

Kolarsky, R. A., P. Mann, and W. Montero, Island arc response to shallow subduction of the Cocos Ridge, Costa Rica, in Geologic and tectonic development of the Caribbean plate boundary in southern Central America, edited by P. Mann, *Spec. Pap. Geol. Soc. Am.*, *295*, 235–262, 1995.

Korenaga, J., and P. B. Kelemen, Major element heterogeneity in the mantle source of the North Atlantic igneous province, *Earth Planet. Sci. Lett.*, *184*, 251–268, 2000.

Korenaga, J., W. S. Holbrook, G. M. Kent, P. B. Kelemen, R. S. Detrick, H.-C. Larsen, J. R. Hopper, and T. Dahl-Jensen, Crustal structure of the southeast Greenland margin from joint refraction and reflection seismic tomography, *J. Geophys. Res.*, *105*, 21,591–21,614, 2000.

Korenaga, J., W. S. Holbrook, R. S. Detrick, and P. B. Kelemen, Gravity anomalies and crustal structure at the southeast Greenland margin, *J. Geophys. Res.*, *106*, 8853–8870, 2001.

Korenaga, J., P. B. Kelemen, and W. S. Holbrook, Methods for resolving the origin of large igneous provinces from crustal seismology, *J. Geophys. Res.*, *107*(B9), 2178, doi:10.1029/2001JB001030, 2002.

Langmuir, C. H., E. M. Klein, and T. Plank, Petrological systematics of mid-ocean ridge basalts: Constraints on melt generation beneath mid-oceanic ridges, in *Mantle Flow and Melt Generation at Mid-Oceanic Ridges*, *Geophys. Monogr. Ser.*, vol. 71, edited by J. Phipps-Morgan, D. K. Blackman, and J. M. Sinton, pp. 183–280, AGU, Washington, D. C., 1992.

Lonsdale, P., and K. D. Klitgord, Structure and tectonic history of the eastern Panama Basin, *Geol. Soc. Am. Bull.*, *89*, 981–999, 1978.

Maclennan, J., D. McKenzie, and K. Gronvold, Plume-driven upwelling under central Iceland, *Earth Planet. Sci. Lett.*, *194*, 67–82, 2001.

Marcaillou, B., P. Charvis, J.-Y. Collot, E. Flueh, and J. Bialas, Deep structure of the Malpelo Ridge (Colombia) from seismic and gravity modeling, paper presented at XVI EGS General Assembly, Eur. Geophys. Soc., Nice, France, 2001.

Matarese, J. R., Nonlinear traveltime tomography, Ph.D. thesis, Mass. Inst. of Technol., Cambridge, 1993.
McKenzie, D., and M. J. Bickle, The volume and composition of melt generated by extension of the lithosphere, *J. Petrol.*, *29*, 625–679, 1988.
Morgan, J. V., P. J. Barton, and R. S. White, The Hatton Bank continental margin-III. Structure from wide-angle OBS and multichannel seismic refraction profiles, *Geophys. J. Int.*, *98*, 367–384, 1989.
Morgan, W. J., Rodriguez, Darwin, Amsterdam, . . ., A second type of hotspot island, *J. Geophys. Res.*, *83*, 5355–5360, 1978.
Morton, J. L., and N. H. Sleep, A mid-ocean ridge thermal model: Constraints on the volume of axial hydrothermal heat flux, *J. Geophys. Res.*, *90*, 11,345–11,353, 1985.
Moser, T. J., Shortest path calculation of seismic rays, *Geophysics*, *56*, 59–67, 1991.
Moser, T. J., G. Nolet, and R. Snieder, Ray bending revisited, *Bull. Seismol. Soc. Am.*, *82*, 259–288, 1992.
Mutter, C. Z., and J. C. Mutter, Variations in thickness of layer 3 dominate oceanic crustal structure, *Earth Planet. Sci. Lett.*, *117*, 295–317, 1993.
Parker, R. L., The rapid calculation of potential anomalies, *Geophys. J.R. Astron. Soc.*, *31*, 447–455, 1972.
Parsons, B., and J. G. Sclater, An analysis of the variation of ocean floor bathymetry and heat flow with age, *J. Geophys. Res.*, *82*, 803–827, 1977.
Pennington, W. D., Subduction of the eastern Panama Basin and seismotectonics of northwestern South America, *J. Geophys. Res.*, *86*, 10,753–10,770, 1981.
Plank, T., and C. H. Langmuir, Effects of melting regime on the composition of the oceanic crust, *J. Geophys. Res.*, *97*, 19,749–19,770, 1992.
Ribe, N. M., The dynamics of plume-ridge interaction: 2. Off-ridge plumes, *J. Geophys. Res.*, *101*, 16,195–16,204, 1996.
Sallarès, V., and P. Charvis, Crustal thickness constraints on the geodynamic evolution of the Galapagos volcanic province, *Earth. Planet. Sci. Lett.*, *214*, 545–559, 2003.
Sallarès, V., P. Charvis, E. R. Flueh, J. Bialas, and C. Walther, Wide-angle seismic constraints on the evolution of Galapagos hotspot-Cocos-Nazca spreading center interaction, paper presented at EGS XXVII General Assembly, Eur. Geophys. Soc., Nice, France, 2002.
Sandwell, D. T., and W. H. F. Smith, Marine gravity anomaly from Geosat and ERS-1 satellite altimetry, *J. Geophys. Res.*, *102*, 10,039–10,054, 1997.
Schilling, J.-G., Upper mantle heterogeneities and dynamics, *Nature.*, *314*, 62–67, 1985.
Schilling, J.-G., Fluxes and excess temperatures of mantle plumes inferred from their interaction with migrating mid-oceanic ridges, *Nature*, *352*, 397–403, 1991.
Schilling, J.-G., H. Kingsley, and J. D. Devine, Galapagos hotspot-spreading center system: 1. Spatial petrological and geochemical variations (83°–101°W), *J. Geophys. Res.*, *87*, 5593–5610, 1982.
Schilling, J. G., M. Zajac, R. Evans, T. Johnson, W. White, J. D. Devine, and R. Kingsley, Petrological and geochemical variations along the Mid-Atlantic ridge from 29°N to 73°N, *Am. J. Sci.*, *283*, 510–586, 1983.
Sleep, N. H., Hotspots and mantle plumes-some phenomenology, *J. Geophys. Res.*, *95*, 6715–6736, 1990.
Tarantola, A., *Inverse Problem Theory: Methods for Data Fitting and Model Parameter Estimation*, 613 pp., Elsevier Sci., New York, 1987.
Tarantola, A., and B. Valette, Inverse problems: Quest for information, *J. Geophys.*, *50*, 159–170, 1982.
Toomey, D. R., and G. R. Foulger, Tomographic inversion of local earthquake data from the Hengill-Grensdalur central volcano complex, Iceland, *J. Geophys. Res.*, *94*, 17,497–17,510, 1989.
Toomey, D. R., E. E. Hooft, and R. S. Detrick, Crustal thickness variations and internal structure of the Galapagos Archipelago, *Eos Trans. AGU*, *82*(47), Fall Meet. Suppl., Abstract T42B-0939, 2001.
Trummer, I., E. R. Flueh, and the PAGANINI Working Group, Seismic constraints on the crustal structure of Cocos Ridge off the coast of Costa Rica, *Neues Jahrb. Geol. Palaentol.*, *225*(1), 25–37, 2002.
Walther, C., Crustal structure of the Cocos Ridge northeast of Cocos Island, *Panama Basin, Geophys. Res. Lett.*, *29*(20), 1986, doi:10.1029/2001GL014267, 2002.
White, R. S., and D. McKenzie, Magmatism at rift zones: The generation of volcanic continental margins and flood basalts, *J. Geophys. Res.*, *94*, 7685–7794, 1989.
White, R. S., and D. McKenzie, Mantle plumes and flood basalts, *J. Geophys. Res.*, *100*, 17,543–17,585, 1995.
White, R. S., D. McKenzie, and R. K. O'Nions, Oceanic crustal thickness from seismic measurements and Rare Earth Element inversions, *J. Geophys. Res.*, *97*, 19,683–19,715, 1992.
Wilson, D. S., and R. N. Hey, History of rift propagation and magnetization intensity for the Cocs-Nazca spreading center, *J. Geophys. Res.*, *100*, 10,041–10,056, 1995.
Zhang, J., and M. N. Toksöz, Nonlinear refraction travel time tomography, *Geophysics*, *63*, 1726–1737, 1998.

J. Bialas and E. R. Flueh, Geomar, Research Center for Marine Geosciences, 1–3 Wischhofstrasse, D-24148 Kiel, Germany. (jbialas@geomar.de; eflueh@geomar.de)

P. Charvis and V. Sallarès, Institut de Recherche pour le Développement (IRD), Géosciences Azur, B.P. 48, F-06235 Villefranche-sur-mer, France. (charvis@obs-vlfr.fr; sallares@obs-vlfr.fr)